

Ninety-Seven New Variable Stars in ω Centauri

Douglas Walker

Department of Mathematics, Embry-Riddle University Worldwide; walked35@erau.edu

Michael Albrow

Department of Physics and Astronomy, Private Bag 4800, University of Canterbury, Christchurch, New Zealand; michael.albrow@canterbury.ac.nz

Received February 19, 2023; revised June 19, 2023; accepted June 29, 2023

Abstract High-cadence photometry of the globular cluster NGC 5139 (ω Centauri) was conducted using the ULTRACAM high-speed frame transfer CCD camera at the 8.2-m Very Large Telescope (VLT) at La Silla, Chile. This research employs difference imaging algorithms to produce time-series photometry data to search for new variable stars within the ω Centauri cluster. The search produced the detection of 117 variable type stars, 19 which were identified and recovered from earlier surveys. An additional set of checks against the Strasbourg astronomical Data Center (CDS) and *General Catalogue of Variable Stars* (GCVS database, Version 2022 June) listed 20 entries, 10 of which were listed as either Horizontal Branch (HB) or Red Giant Branch Stars but not as variables. A single star identified in the CDS is listed as a new RR Lyrae variable. Removing these counts from the 117 identified variables leaves 97 previously unidentified variable stars in ω Centauri. This new variable list includes 5 possible new RR Lyrae types, 13 eclipsing binary type systems, 11 BY Draconis, 3 SX Phoenicis, and 65 variables which have been identified as unknown general Irregular/Semiregular type variables.

1. Introduction

NGC 5139, also known as omega Centauri (ω Cen), is a globular cluster (GC) in the constellation of Centaurus visible from the southern hemisphere. ω Centauri had been listed in Ptolemy's catalog as a star and it was Edmond Halley who was the first to document its nonstellar nature in 1677 by listing it as a "luminous spot or patch in Centaurus" in his historical list of six such objects. Lacaille included it in his catalog as number I.5.

NGC 5139 is located at R.A. $13^{\text{h}} 26^{\text{m}} 47.28^{\text{s}}$, Dec. $-47^{\circ} 28' 46.1''$, has a heliocentric radial velocity of 231.1 km/s, distance modulus of 13.94, and a [Fe/H] value of -1.53 (Harris 1996). It is the biggest of all globular clusters in the Milky Way galaxy, being about 10 times as massive as other globular clusters and containing about the same mass as the smallest whole galaxies. It is also the most luminous Milky Way globular, and the brightest globular cluster in the sky. In the Local Group, it is outshone only by the brightest globular cluster G1 in the Andromeda Galaxy M31. NGC 5139 may not actually be a classical globular cluster but instead a remnant of a dwarf galaxy that has merged with the Milky Way (Bekki and Freeman 2003).

NGC 5139 contains a dense concentration of variable stars with only the cluster M3 surpassing it in total number of variables. Bailey (1902) identified 128 variables in the cluster and by 1938, 161 variables had been identified by Martin (1938). The catalog of Sawyer Hogg (1973) provided data for variables V1-V183, where four stars were deemed to be non-variable and therefore excluded from the data set. The number was increased by 83 variables as a result of the study of Niss *et al.* (1978). Additional new and suspected variables have been reported by Dickens *et al.* (1972), Fourcade *et al.* (1978), Jorgensen and Hansen (1984), and Mukherjee *et al.* (1992). Currently, the identified number of variables in the cluster is 460 (Clement 2017). Recent publications have focused on the

populations of RR Lyraes (e.g. Magurno *et al.* (2018), Braga *et al.* (2018), Braga *et al.* (2016), Navarrete *et al.* (2015)) and near-IR period-luminosities (e.g. Navarrete *et al.* (2017)).

2. Observations

Observational time series data for this project were collected over six observing nights from 22 to 27 April 2011 at the European Southern Observatory's 8.2-m Very Large Telescope on Cerro Paranal in the Atacama Desert of northern Chile. A total of eight observation runs over the six nights with a frame-rate of 6 Hz were obtained. Each observation run contains between 90 and 320 exposures. Image data were acquired using ULTRACAM, an ultra-fast, triple-beam CCD camera designed to provide imaging photometry at high temporal resolutions. The CCDs in ULTRACAM are E2V 47-20 frame-transfer devices of cosmetic quality (grade 0) and quantum efficiency. The chips are Peltier and water-cooled to 233 K, giving approximately 0.05 electron/pixel/second dark current. The readout noise of the chips is low at just over 3 electrons when reading out at 10 microseconds/pixel and just under 6 electrons when reading out at 2 microseconds/pixel (Dhillon *et al.* 2007). The SDSS photometric system (Fukugita *et al.* 1996) was adopted as the primary filter set for ULTRACAM. This system consists of five color filter bands (u', g', r', i', and z').

ULTRACAM contains two CCD chips. The CCD chip FOV coverage for NGC 5139 is a region from the outer edge to the inner part of the cluster as shown in Figure 1.

Area coverage for detectors 1 and 2 is shown along with a scale marker, orientation, and half-light radius in Figure 1. The FOV covers a sky patch approximately 5×5 arcmin² at a scale of 0.3 arcsec pixel⁻¹, comprising the two CCD chips where each chip contains 1024 pixels on a side. Telescope pointing was located off the center of the cluster at R.A. $13^{\text{h}} 27.0^{\text{m}} 07.46^{\text{s}}$ and Dec. $-47^{\circ} 032.0' 46.110''$. The FOV

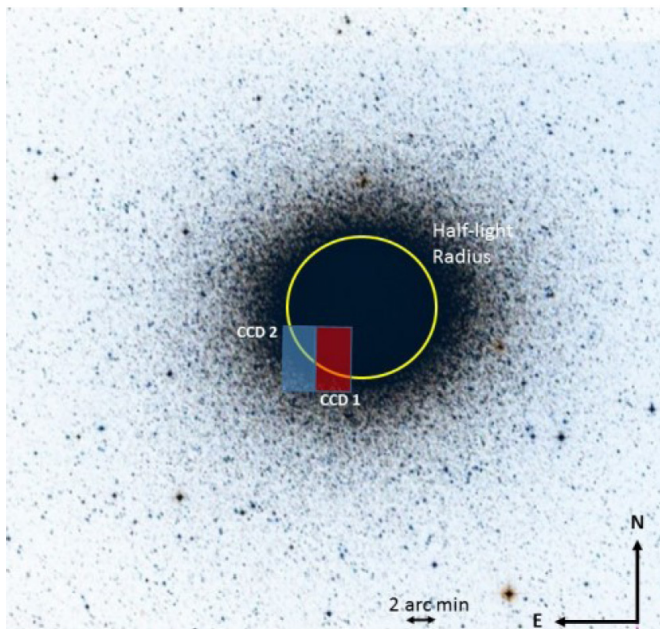


Figure 1. ULTRACAM science camera FOV for NGC 5139.

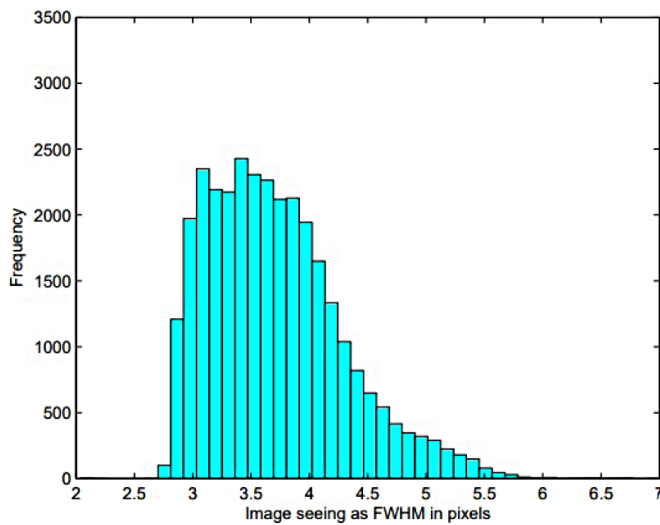


Figure 2. Image seeing as FWHM in pixels for u' filter band.

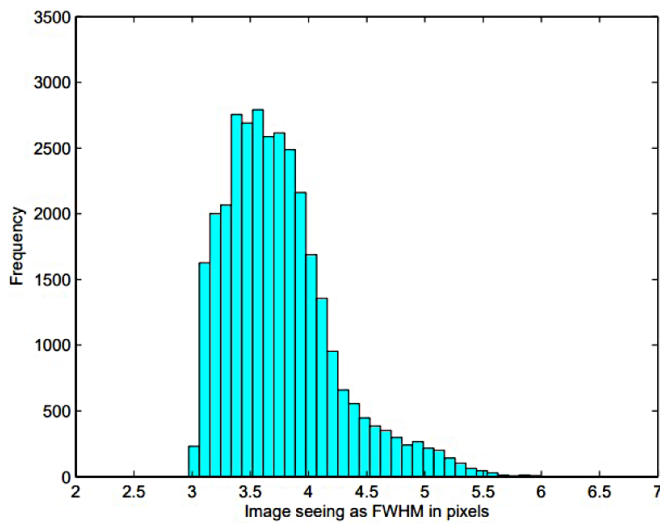


Figure 3. Image seeing as FWHM in pixels for g' filter band.

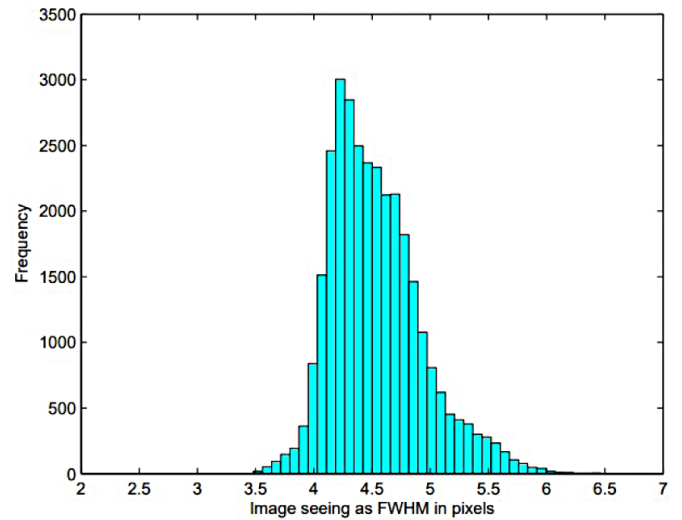


Figure 4. Image seeing as FWHM in pixels for r' filter band.

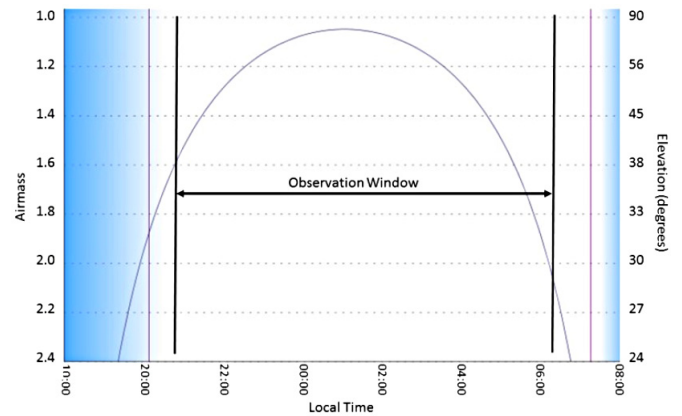


Figure 5. Air mass and observation window for NGC 5139 ULTRACAM.

covered by VLT is from R.A. $13^{\text{h}} 26^{\text{m}} 49.70^{\text{s}}$ to $13^{\text{h}} 27^{\text{m}} 07.50^{\text{s}}$ and Dec. $-47^{\circ} 029.00' 45.300''$ to $-47^{\circ} 035.00' 46.500''$ for the detector CCD1. Likewise for detector CCD2, the coverage area is R.A. $13^{\text{h}} 27.0^{\text{m}} 07.50^{\text{s}}$ to $13^{\text{h}} 27.0^{\text{m}} 25.30^{\text{s}}$ with the same coverage for Dec.

Images were collected over the three filter bands of SDSS u' filter (300–400 nm), SDSS g' filter (400–540 nm), and SDSS r' filters (540–700 nm).

Photometric conditions for images given in Full Width Half Maximum (FWHM) pixels are given in Figures 2 through 4 for filters u', g', and r', respectively. As period searching and analysis was conducted over a combined set of data and not on single observation days, histograms of seeing conditions are given over the complete data set.

The median FWHM for the u' and g' filters is approximately 3.5 pixels. The r' filter conditions were somewhat worse at 4.5 pixels. Combined airmass reading covering the observation cycle was calculated using the on-line tool TAPIR as shown in Figure 5. Optimum observation times were between 22:00 and 04:00 hours local time, which is at minimum airmass. As shown in Figure 5, the observations covered approximately the complete observing cycle.

3. Data reduction and light curve generation

In order to prepare the collected image frames for the discovery steps of new variable star detection and corresponding verification, a series of processing steps was executed. These steps include image preprocessing, image registration, reference image generation, image subtraction, and finally light curve generation, which includes detrending and positional correlation.

To extract photometry from the time-series images, the data frames were initially put through a standard calibration pipeline which involved bias and dark subtraction and flat-field correction. Initial data reduction consisted of splitting the FITS images into separate CCD1/2 detector images and performing cosmic ray removal using the Laplacian edge detection cosmic removal algorithm (van Dokkum 2001).

A detailed sequence flow to carry out the difference image and light curve generation for the GCs was created which included the input/output conditions between discrete steps. Initial inputs into the processing flow consisted of the VLT image data, and outputs were corrected light curves ready for applications of variable star search techniques. Major processing steps are indicated by the gray boxes shown in Figure 8. The process flow was generic and accommodated both the Bramich (2008) and (2013) algorithm implementations.

3.1. Difference image analysis

The Difference Image Analysis (DIA) method attempts to match one image to another by deriving a convolution kernel describing the changes in the Point Spread Function (PSF) between images. When applied to time-series data with a high signal-to-noise reference image, the differential photometry approach regularly provides superior precision to more traditional profile-fitting photometry methods. Achieving errors close to the theoretical Poisson limit is possible. Moreover, DIA is the only reliable way to analyze the most crowded stellar fields (Bramich 2008). The potential of DIA as a powerful tool for unveiling short period variable stars or small amplitude variations in Blazhko RR Lyrs in the densely populated central regions of GCs has been demonstrated in Kains *et al.* (2012), Arellano Ferro *et al.* (2012), Bramich *et al.* (2011), Corwin *et al.* (2006), and Strader *et al.* (2002).

DIA using the PySIS3 code (Albrow 2017) was used to obtain high-precision photometry of the point sources. A stacked reference image was produced in each band by selecting the best-seeing images (500 images for u' band, 500–1000 images for g' and r' bands), taking care to minimize the number of saturated stars. The resulting reference image in the u' filter consists of a single image with an exposure time of 3000s, and FWHM of the point spread function (PSF) of 4.0–4.2 pixels. In the g' band, the reference image is made from stacked images with a total exposure time of 6000s and a PSF FWHM of 3.9–4.0 pixels. In the r' band, the reference image is again made from stacked images with a total exposure time of 6000s and a PSF FWHM of 1.7–4.0 pixels. The reference image, convolved with the kernel solution, is subtracted from each of the time-binned images to create difference images, and, in each difference image, the differential flux for each star is measured by scaling the PSF at the position of the star.

Because of the way difference imaging works, measured reference fluxes of a star on the reference image might be systematically too large due to contamination from other nearby point objects. Non-variable sources are fully subtracted on the difference images and as such, this problem does not occur for detection of variable stars. Variable sources with overestimated reference fluxes will have an underestimated variation amplitude. Once DIA was completed, DAOphot was used to detect and measure the magnitude of the stars in the reference images (Stetson 2015). The star positions, magnitudes, and associated statistics were used as inputs into the light curve generation process.

3.2. Light curve generation

Light curves for all identified stars were achieved by transforming the reference star list to image coordinates and performing PSF photometry on the residual image at the location of the transformed stars. Differential light curves were generated in all three bands for a total of 1451 curves in the u' band, 5267 in the g' band, and 5727 in the r' band.

For the VLT time series data, differential light curves were generated in the u', g', and r' filter bands using the modified PySIS3 code. Independent reference images were created for each band utilizing different combinations of images which are co-aligned. Stars were detected independently on each of the three reference images such that each filter has its own list of stars. Light curves were generated for all stars that were identified in each filter band.

Table 1 lists the light curves for the three filters for a total of 15,629 light curves in the u' band, 14,950 light curves in the g' band, and 9,156 light curves in the r' band. Cross-referencing stars across filter bands, light curves in one or more filters were generated for 24,106 individual stars.

Table 1. Generated light curves for NGC 5139.

<i>Filter</i>	<i>CCD Detector</i>	<i>No. Light Curves</i>
u'	1	8,917
	2	6,712
g'	1	10,120
	2	4,830
r'	1	3,532
	2	5,624
Total		24,106

3.3. Detrending of data

Noise in signals is the result of effects such as 1) instrumentation: focus, drift, electronic noise, pointing tweaks, and even thermal effects; 2) atmospheric: extinction and turbulence; and 3) astronomic: cosmic rays. The image subtraction process removes some of the noise components but others remain. Additional correlated trends in the light curve data can be removed by detrending techniques. Multiple methods are available for detrending. These include the boxcar moving average smoothing algorithm where a sliding moving average is used to smooth the data which is subtracted from the original curve. This takes out the low-frequency trends

but leaves the higher-frequency changes in the flux in place. Other techniques include the Savitzky and Golay (1964) (S-G) smoothing algorithm. The idea behind S-G is that it also uses a sliding window along the light curve, but instead of computing a moving average, it performs a polynomial regression fit. Other techniques include RC circuit (high and low pass filter) and Fast Fourier Transforms (FFTs). The technique utilized in this research is the Trend Filtering Algorithm (TFA) (Kovács *et al.* 2005). TFA assumes that a substantial portion of the large number of stars in the target space are non-varying. See Walker (2016) for a detailed mathematical derivation.

The number of template stars used was dependent on the individual case. The total number of template stars used for the light curves being corrected typically ranged from 50 to 100 stars. Plots of star magnitudes vs. the RMS of the light curves were generated to determine the range of correction. An example of detrended data set for the g' band is shown in Figure 6.

3.4. Color magnitude diagrams

The Hertzsprung-Russell (HR) diagram plots log luminosity vs. log temperature (or absolute magnitudes vs. spectral types). Color Magnitude Diagrams (CMDs) are a variant of the HR diagram dedicated to the study of star clusters. A CMD is a scatter graph showing the relationship between each object's absolute magnitude and its estimated surface temperature or between optical or perceptual proxies for these quantities. Plots of CMDs are particularly useful in the study of GCs.

Before utilizing the CMDs in analysis, it is important that the generated CMDs are calibrated with a standard photometry catalog. For each GC data set, a calibrated catalog of stars for that GC in the $UBVR_{\text{c}}I_{\text{c}}$ system was acquired from the Photometric Standard Fields in the Canadian Astronomy Data Centre (CADC) (Stetson 2015).

CMDs for the fields under analysis were generated as follows. A calibrated catalog of over 140,000 stars in the $UBVR_{\text{c}}I_{\text{c}}$ system was provided by Bono (2015). The transformation provided by Chonis and Gaskell (2008) was used to transform values from the Johnson/Cousins to the SDSS system in order to match the generated color differences to those provided in the catalog data set.

A calibration to the catalog system was performed by first selecting a subset of stars with comparable magnitudes from both sets. Using World Coordinate System (WCS) reference coordinates, matching stars were found in both data sets. A statistical average of the color magnitude difference was calculated for the selected stars in all three color bands. This average was applied to all stars and differences used to generate corresponding CMDs. CMD plots for the data sets plotted on top of the catalog data are shown in Figure 7. Green color points represent the calibration data set, while the cyan color data points are the generated band differences. A greater number of overlap of stars identified in the g' and r' bands results in a larger number of stars plotted on the $g'-r'$ vs g' plot compared to the $u'-g'$ vs u' plot. The $g'-r'$ vs g' shows a few stars in the split sequence which is clearly visible in the catalog data set.

The black lines in Figure 7 represent the theoretical stellar isochrone for this cluster. The Dartmouth Stellar Evolution

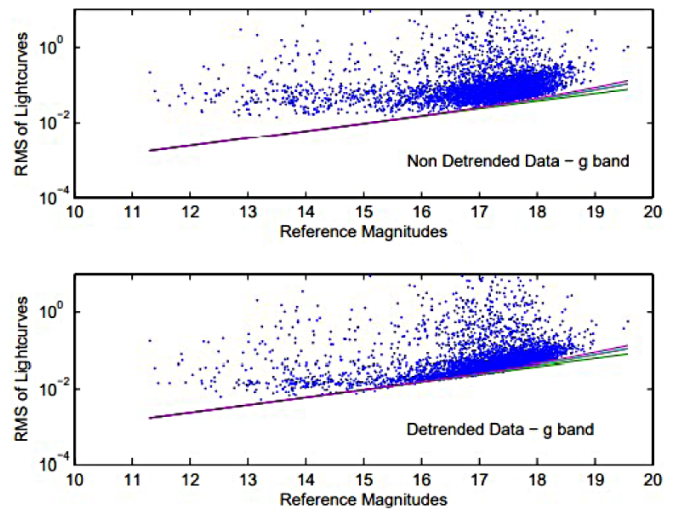


Figure 6. Example of detrended data set for g' . Top panel: RMS of light curves which have not been detrended. Bottom panel: RMS of light curves after detrending. Plotted in the figure are the readout noise (lower green line) and the Poisson noise (red and blue lines) with and without the mean sky background added, respectively.

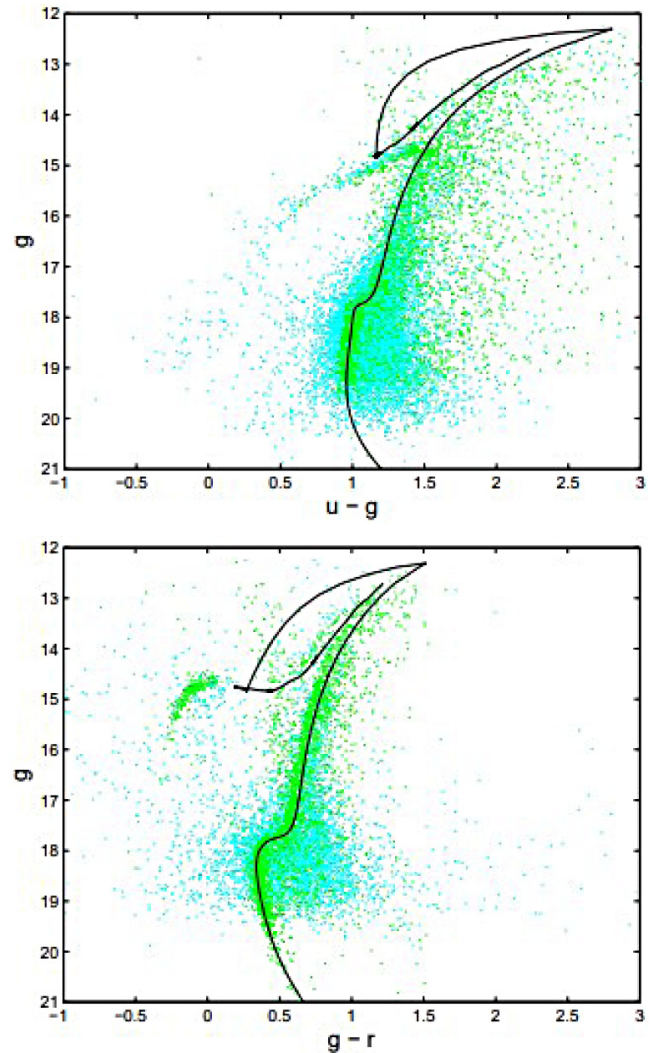


Figure 7. Calibrated Color Magnitude Diagrams. top-panel: u' vs $u'-g'$; bottom-panel: g' vs $g'-r'$. Green color points represent the calibration data set while the cyan color data points are the statistical average for the generated band differences as described. The black lines is the stellar isochrone.

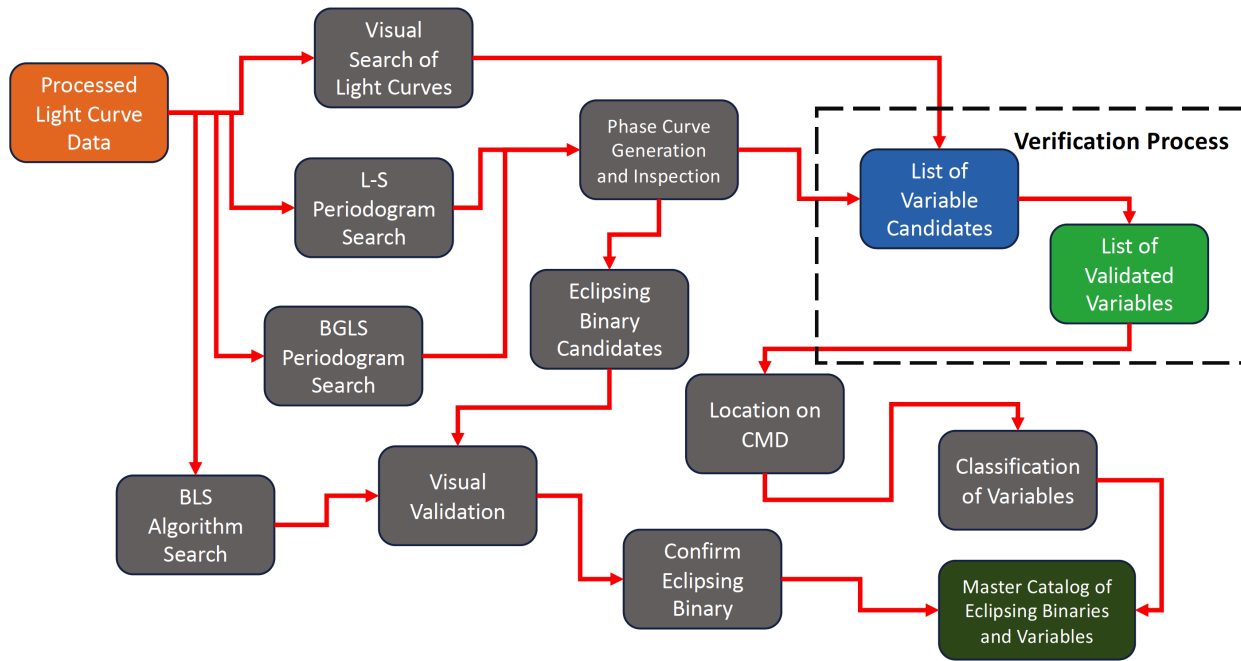


Figure 8. Variable star and eclipsing binary search processing flow.

Database 2 was used to generate the isochrones for this study. The fit of the isochrone to the photometry is to a first approximation only and is used for general location of variables. The fit was achieved in a two-step process. A pixel shift was first used to closely align the isochrone to the main sequence in the photometry. Once an alignment was completed, a least-squares fit was used to minimize the isochrone line to the mean of the photometry data. The isochrones generated used an alpha-enhanced chemical mixture.

The isochrone from the base of the main sequence through to the tip of the giant branch is designated as the Main Sequence Giant Branch Ridge Line (MSGBRL).

4. Variable star search algorithms

A set of variable star search algorithms was utilized in the search methodology. For searches for variable star demonstrating periodicity these included the Lomb-Scargle (L-S) periodogram (Scargle 1982), Bayesian Generalized Lomb-Scargle (BGLS) Periodogram (Mortier *et al.* 2015), and the Phase Dispersion Minimization (PDM) method (Stellingwerf 1978). For eclipsing type systems, algorithms included Box Least Squares (BLS) (Kovács *et al.* 2002) and the Plavchan periodogram (Plavchan *et al.* 2008).

Using these periodic search algorithms and complementing with visual search techniques, a series of steps are executed taking the light curve data and producing a candidate list of variables. All major process steps are detailed below and illustrated in the process flow shown in Figure 8.

All light curve time series data are first processed through the L-S and BGLS search algorithms, producing a list of potential variable star candidates. A cursory inspection is performed on the corresponding set of phased light curves produced with the periods found in the search algorithms. If an eclipsing binary

is suspected, the candidate is separated for additional analysis. The original light curves are also passed through the BLS search algorithm for possible Detached Eclipsing Binaries (DEBs). In addition, a rapid visual examination of the raw light curves is conducted looking for candidate variable stars which may not be periodic in nature. If candidates are found, they are sent to the verification process, as shown in Figure 8. Once a list of variable star candidates is generated, it is submitted to a series of verification steps that are contained in the dotted box in Figure 8. By processing the candidate list through these verification steps (multiple iterations are required), a strict quality control approach for inclusion of variables and DEBs into the final GC variable candidate list is followed, ensuring a high level of confidence that identified variable stars are actually varying.

4.1. Analysis for validation of variability

A confidence validation step was performed to show that the detection of stellar variability was above certain threshold levels, providing a high confidence level that actual stellar variability is occurring. A decision analysis approach was utilized using a Simple Additive Weighting (SAW) method. The outcome from the SAW process resulted in a confidence rating of variables based on where the variable resides in a specific confidence level which is generated on the weighted inputs from the process steps.

Inputs to the SAW algorithm were based on measures from the following:

- Signal-to-Noise Ratio (SNR)
- RMS values of all stars across all filter bands
- Cross-correlations between filter bands
- Cross-correlation to nearby stars
- Stetson Variability Index
- Period comparison to window aliasing

The Signal-to-Noise Ratio is classically defined as the ratio of the power of a signal (meaningful information) to the power of background noise (unwanted signal). The simplest form is:

$$\text{SNR} = P_{\text{signal}} / P_{\text{noise}} \quad (1)$$

where P is average power. Both signal and noise power must be measured at the same or equivalent points in a system, and within the same system bandwidth. A ratio higher than 1:1 indicates more signal than noise. As described above, the SNR as used in all analysis and recorded on all plots is defined as:

$$\text{SNR} = \text{signalamplitude} / X_{\text{RMS}} \quad (2)$$

The Root Mean Square, also known as the quadratic mean in statistics, is a statistical measure defined as the square root of the mean of the squares of a sample (Bird 2007).

For the SNR of the 117 variables, the numbers ranged from a value of 0.234 to 4.401. Measuring the amplitude in magnitudes of the fitted sinusoidal phases, the SNR of the phased light curves were generated and plotted. The RMS values of all stars across all filters as a function of magnitude were generated. Examining these results shows that the majority of variables with magnitudes brighter than 17 have a RMS value greater than the 1σ value of the set of stars that are found within 0.1 magnitude of the target star. Variables which have strong variability compared to other stars within a magnitude band should have values above the one sigma range. Conversely, stars that do not show variability to other stars within that 0.1-magnitude band will fall close to the mean of the set and within the 1σ bounds.

Cross-correlations between filter bands were calculated at zero-lag due to phase differences being generally restricted to $\pm 10\%$ between filters. These cross-correlations between filter bands ranged from very weak to strong. Examination of the cross-correlation results indicates that while many variables have zero lag values greater than the 1σ range of the companion magnitude stars, many have values below the mean and some even below the lower end of the 1σ range.

To validate that the variability in the primary filter band is not an artifact of the image detector or the difference image processing, the cross-correlation of the variable star and a set of nearby stars in that filter band within a defined pixel radius was performed. The autocorrelation values for all the variables at zero lag is 1. All variables in the g' filter, all except one have mean cross-correlation values of nearby stars less than 0.6. The values for the variables in the r' have a wider sigma range, with the highest value being 0.8 and the mean value of the nearby stars approximately 0.55. For the u' filter, values are 0.4 or below.

The Stetson Variability Index (SVI) statistic has been widely used to characterize variability in multiwavelength observations (Carpenter *et al.* 2001; Rice *et al.* 2012). Since it accounts for the correlated changes in multiband magnitudes, the Stetson index can be used to identify variables with relatively low variability compared with photometric errors.

The basic idea behind the SVI is that if a star is truly variable, independent time series observations taken closely in time should consistently agree more closely, on average, than observations taken further apart. This distinguishes variability from noise and image defects, such as cosmic rays.

Numeric inputs to SAW are the values generated from the SNR, RMS, cross-correlation, and SVI analysis processes. These numeric inputs were generated directly from the analytical MATLAB programs. The inputs for the visual analysis are subjective and as such, are inherently uncertain, as they depend on interpretation and knowledge. After investigations for the optimum set of weights, the values assigned to the associated inputs for the VLT data are shown in Figure 9. The visual, SNR, and cross-correlation between filter bands were considered the most important parameters. The RMS and SVI are closely associated with the SNR and cross-correlation respectively, thus they are assigned smaller weight values.

Applying this approach to all 117 detected variables results in the confidence rating bands as shown in Figure 10. The tabular listing for each variable and its confidence rating is in Table 2.

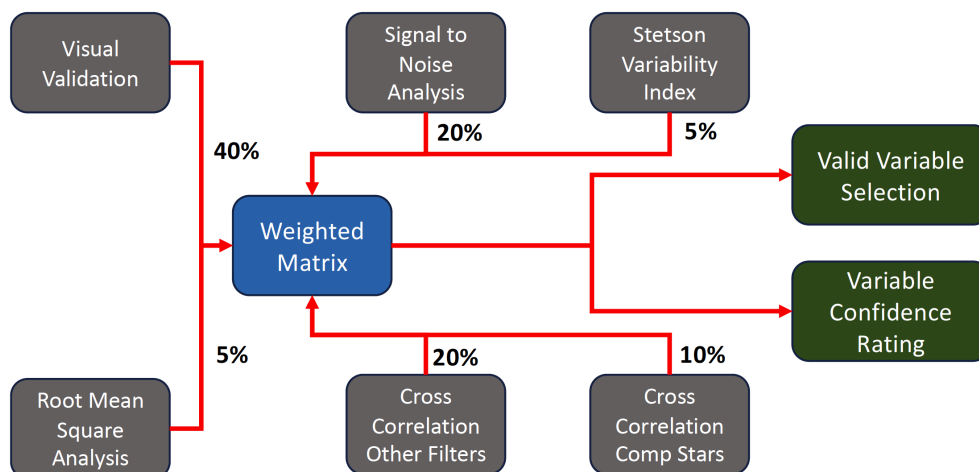


Figure 9. Variable star selection and verification processing flow. Percentages represent the weighted values of the inputs into the matrix.

4.2. Recovery of known variables

In order to determine the efficiency of the detection algorithms and approaches, a concentrated effort was made to recover the known variables in the ULTRACAM CCD detector FOVs which have been published in the literature and listed on astronomical databases.

Once the GC variables were identified, the x,y pixel positions from the reference image were mapped to J2000 R.A. and Dec. coordinates. After these coordinates were obtained, they were checked against the *Catalogue of Variable Stars* (Clement 2017). In addition, the list of coordinates was checked utilizing both the SIMBAD Astronomical Database and the AAVSO International Variable Star Index (VSX) coordinate query with a search radius of 1.5 arc sec around the targets. Cross-referencing these lists, the variables displayed in Table 3 have been recovered from earlier surveys.

Table 3 lists the variables survey ID from this survey, the corresponding ID obtained from the SIMBAD Astronomical Database, the identified variable type, ICRS coordinates, identified period from the search algorithm, and magnitudes in the SDSS u', g', r' filters as well as the B and V filters from the SIMBAD website.

4.2.1. Search detection efficiency

The list in Table 3 was generated by comparing the FOV with earlier surveys which generated a total of 32 variables which had been identified in the VLT FOV. The search space

Table 2. Confidence level of variables.

ID	Confidence	ID	Confidence	ID	Confidence
5139 No.	Level	5139 No.	Level	5139 No.	Level
5139v-1	EH	5139v-40	H	5139v-79	H
5139v-2	H	5139v-41	M	5139v-80	H
5139v-3	H	5139v-42	H	5139v-81	L
5139v-4	EH	5139v-43	H	5139v-82	H
5139v-5	M	5139v-44	H	5139v-83	M
5139v-6	H	5139v-45	L	5139v-84	M
5139v-7	H	5139v-46	H	5139v-85	M
5139v-8	M	5139v-47	H	5139v-86	M
5139v-9	L	5139v-48	H	5139v-87	L
5139v-10	L	5139v-49	M	5139v-88	L
5139v-11	EH	5139v-50	M	5139v-89	L
5139v-12	M	5139v-51	EH	5139v-90	M
5139v-13	H	5139v-52	H	5139v-91	M
5139v-14	H	5139v-53	H	5139v-92	H
5139v-15	H	5139v-54	M	5139v-93	L
5139v-16	H	5139v-55	H	5139v-94	M
5139v-17	H	5139v-56	H	5139v-95	L
5139v-18	M	5139v-57	H	5139v-96	M
5139v-19	H	5139v-58	H	5139v-97	M
5139v-20	H	5139v-59	EH	5139v-98	L
5139v-21	M	5139v-60	H	5139v-99	M
5139v-22	H	5139v-61	M	5139v-100	H
5139v-23	H	5139v-62	H	5139v-101	M
5139v-24	M	5139v-63	M	5139v-102	M
5139v-25	L	5139v-64	L	5139v-103	M
5139v-26	M	5139v-65	H	5139v-104	L
5139v-27	H	5139v-66	L	5139v-105	L
5139v-28	H	5139v-67	H	5139v-106	M
5139v-29	H	5139v-68	M	5139v-107	M
5139v-30	H	5139v-69	L	5139v-108	L
5139v-31	EH	5139v-70	H	5139v-109	L
5139v-32	EH	5139v-71	H	5139v-110	L
5139v-33	EH	5139v-72	M	5139v-111	M
5139v-34	H	5139v-73	H	5139v-112	M
5139v-35	EH	5139v-74	H	5139v-113	H
5139v-36	H	5139v-75	M	5139v-114	L
5139v-37	H	5139v-76	H	5139v-115	M
5139v-38	M	5139v-77	H	5139v-116	L
5139v-39	M	5139v-78	M	5139v-117	M

Confidence levels: EH, Extremely High; H, High; M, Medium; L, Low

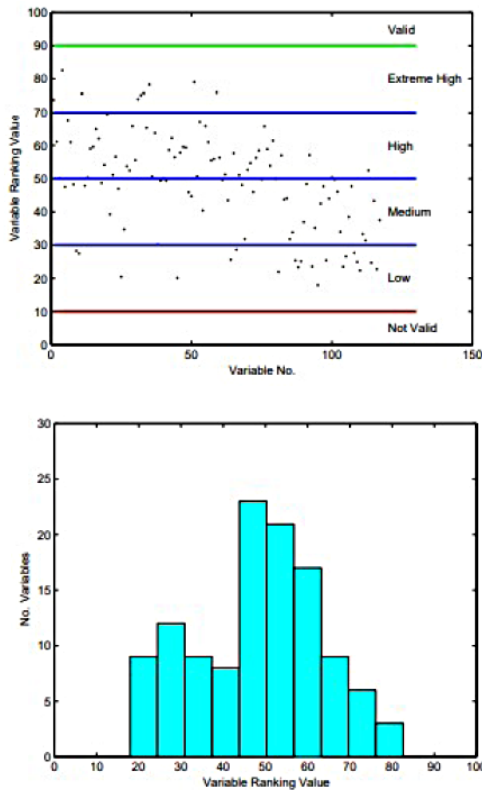


Figure 10. Variable confidence rating. Upper panel: Confidence rating of variables. Lower panel: Histogram of rating values.

was targeted at variables with periods less than one day, which eliminates five variables from the tables that have longer periods. One of the pulsating subdwarf O star (sdOV) variables was not identified in the photometry process so no star was available for light curve analysis. Three of the variables were stars which happen to be chosen as part of the set utilized for detrending of the light curves. These were removed from the detrending process, which leaves 23 variables which could have been recovered. The list in Table 3 shows 20 variables were recovered, producing an overall detection efficiency of 87%. Breaking down specifics: 13 of 13 RR Lyr variables were found for a detection efficiency of 100%, 3 of 4 SX Phe variables were found for a detection efficiency of 75%, and 4 of 4 EA/EB/EW eclipsing systems were found for 100% efficiency. Other variables that were not recovered were the Semiregular (SR) and the sdOV variables.

4.2.2. Analysis of recovered variables

An analysis of a subset of the recovered variables was undertaken to determine the efficiency of the signal processing

Table 3. Recovered variables.

Survey ID	SIMBAD ID - NGC	Type	ICRS Coordinates			Period Days	U'	G'	R'	B	V
			R.A.	Dec.							
			h	m	s	°	'	"			
5139v-1	5139 B V120	RR Lyrae	13 26 25.512	-47 32 49.059	0.36574	15.51	14.62	14.54	15.47	15.03	
5139v-2	5139 BPB 164847	RR Lyrae	13 26 56.529	-47 30 06.196	0.31250	15.07	14.51	14.51	14.88	14.64	
5139v-3	5139 B V41	RR Lyrae	13 27 01.381	-47 31 02.053	0.65741	15.05	14.48	—	14.76	14.63	
5139v-4	5139 B V110	RR Lyrae	13 27 02.050	-47 30 07.052	0.33102	15.17	14.46	14.59	15.26	14.58	
5139v-5	5139 SAW V154	RR Lyrae	13 27 03.119	-47 30 33.085	0.32176	15.04	14.49	14.40	14.88	14.58	
5139v-6	5139 SAW V145	RR Lyrae	13 26 51.213	-47 31 08.850	0.37384	15.26	14.48	—	15.11	14.67	
5139v-7	5139 B V112	RR Lyrae	13 26 54.242	-47 30 23.655	0.47222	15.44	14.69	14.27	15.00	15.03	
5139v-11	5139 BPB 149574	RR Lyrae	13 26 56.177	-47 30 50.578	0.38079	15.17	14.42	14.44	15.02	14.62	
5139v-13	5139 SAW V311	SX Phe	13 26 58.713	-47 29 50.980	0.04149	17.39	—	16.62	17.12	16.79	
5139v-14	5139 SAW V328	SX Phe	13 27 01.259	-47 31 49.940	0.09896	17.69	—	17.17	18.20	17.68	
5139v-16	5139 SAW V298	SX Phe	13 26 50.235	-47 34 03.490	0.03304	17.74	—	17.18	17.73	17.36	
5139v-29	5139 BPB 143269	RR Lyrae	13 27 15.891	-47 31 10.242	0.42245	15.09	14.33	—	14.96	14.43	
5139v-30	5139 SAW V276	RR Lyrae	13 27 16.487	-47 33 18.096	0.30903	15.04	14.47	14.33	14.86	14.59	
5139v-31	5139 NJL 8	RR Lyra	13 27 22.094	-47 30 12.855	0.69213	15.06	14.46	14.15	14.73	14.64	
5139v-32	5139 SAW V365	Variable Star	13 27 11.591	-47 35 02.552	0.47338	15.67	15.19	15.07	15.53	15.29	
5139v-33	5139 B V107	RR Lyrae	13 27 14.027	-47 30 58.388	0.34028	14.93	14.64	14.89	15.92	14.91	
5139v-35	5139 SAW V358	Variable Star	13 27 20.203	-47 31 49.854	0.30002	17.26	16.90	16.82	17.30	17.03	
5139v-37	5139 SAW V337	Eclipsing	13 27 13.776	-47 32 25.030	0.13466	17.53	—	16.87	17.88	17.42	
5139v-38	5139 WSB V68	Eclipsing	13 27 22.950	-47 32 19.100	0.12032	—	—	—	—	17.28	
5139v-60	N[ALJ2017] 255	Red Giant	13 27 14.281	-47 30 59.882	0.33824	—	14.33	—	15.55	14.61	

algorithms and if the variable determination process matched what is recognized in the open literature.

Figure 11 shows the RR Lyr variable identified as 5139 B V120 and has an estimated period of 0.36574 day in the g' band only. Its distinctive shape for a RR Lyr is clearly shown and it has been verified in followup observations taken with a private 1-meter telescope. The magnitude is slightly dimmer in the B and V filters.

Figures 12 and 13 show the phase and light curves for variables identified as eclipsing binary systems according to the SIMBAD Astronomical Database. The estimated periods are 0.13466 and 0.13480 day, respectively. The individual light curves show the frequency of the eclipsing systems better than the phase curves.

Figure 14 shows the distinctive shape of an eclipsing system in which the light curves show both the primary and secondary eclipses and the phase curves shows the secondary eclipse as a shallower eclipse than the primary. The SIMBAD Astronomical Database identifies this eclipsing system as a variable star with no additional references identified. This is clearly an eclipsing system and needs further observation and analysis. At magnitude 16.6 in the g' filter, larger telescope systems will be required to completely resolve the details of the eclipse.

5. Newly discovered variables

Utilizing the search techniques as identified above, 97 new variables in addition to those recovered above were detected across both CCD detectors of the image field. Reviewing the phase and light curves, a variety of variable star classes has been discovered. If we exclude the stars which have been identified as either Red Giant Branch stars or Horizontal Branch stars, we get 78 new detections whose classifications include 14 eclipsing type systems, 8 potential new RR Lyr, 3 SX Phe, 13 BY Dra, and 40 stars which we identify as general pulsating types. If we

include the SIMBAD-designated stars as general pulsating type variables, our detection count increases to 97.

5.1. Validation of variables being newly discovered

In addition to the literature search as described in the introduction, in order to validate that the newly detected variables have not been previously reported in the open literature, a search using the variable coordinates was conducted against both the SIMBAD Astronomical Database and the AAVSO's International Variable Star Index (VSX). The accuracy of stellar positions generated in this study for the recovered variables was collected, resulting in an average of 0.486-arcsecond difference. Based on this, a two-second arcsecond search radius was utilized for checking the list of newly detected variables, which validates the list in Appendix A: Master catalog of detected variable stars. Appendix B contains the master catalog of light curves of all the variable stars.

5.2. Location of discovered variables on CMD

Figures 15 and 16 show the location of a subset of the variables on the CMD. 72 of the 78 variables are analyzed and are located on the CMD. The cyan color data points are the statistical average for the generated band differences as described in section 3.4. A majority of the variables are concentrated along the MSGBRL, as well as many located in the HB, as demonstrated in the u'-g' plot in Figure 15. Figure 16 shows the variables largely scattered across the g'-r' CMD. Variables which lie along the MSGBRL are considered part of the GC while those farther out on the redder and blue regions could possibly be field stars.

Note: Due to the wide scatter of the variables on the g' vs. g'-r' CMD, only the g' vs. u'-g' plot is used for variable location.

5.3. Classification of variables on CMD

Figure 17 shows the location of groups of specific variables

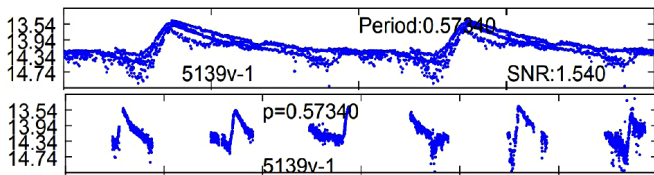


Figure 11. Light curve of RR Lyr SIMBAD 5139 B V120. Top panel: Phase light curve. Bottom panel: Individual light curves over observation periods.

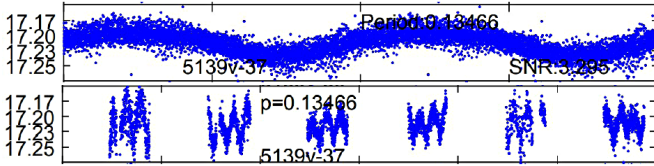


Figure 12. Light curve of Eclipsing system SIMBAD 5139 SAW V337. Top panel: Phase light curve. Bottom panel: Individual light curves over observation periods.

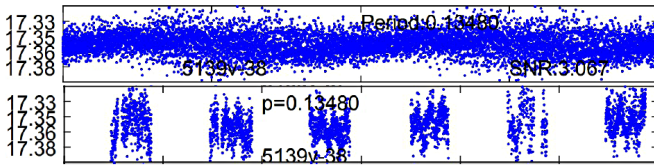


Figure 13. Light curve of Eclipsing system SIMBAD 5139 WSB V68. Top panel: Phase light curve. Bottom panel: Individual light curves over observation periods.

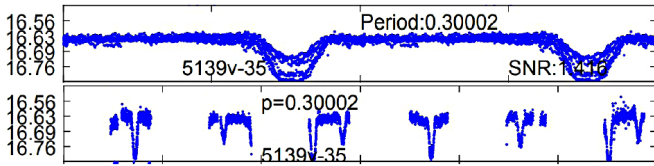


Figure 14. Light curve of variable star SIMBAD 5139 SAW V358. Top panel: Phase light curve. Bottom panel: Individual light curves over observation periods.

on the CMD. As expected, the RR Lyr lie along the HB as indicated by the yellow line. Eclipsing systems (EAs and EBs) are distributed along the MSGBRL with a couple scattered on the HB. BY Dra variables are concentrated in the red box of Figure 17 with the lone exception of variable 5139v-71, which resides in the small red box. The observed g' magnitudes of the BY Dra are consistent for K- or M-type dwarfs. The variable 5139v-71 is possibly a foreground star as it is located too far off the main sequence. It has been given the BY Dra classification based on the light curve characteristic only.

6. Classification of variable stars

This section describes the new variables that have been discovered. For purposes of variable classification, the CMD is divided into four main regions centered on the MSGBRL. A general example is shown in Figure 18.

A corridor region containing the majority of stars concentrated along the MSGBRL was developed in order to separate these stars from the ones in the other defined regions. To develop the corridor boundaries, stars were binned at the one-half magnitude scale. For each bin, the mean and sigma values

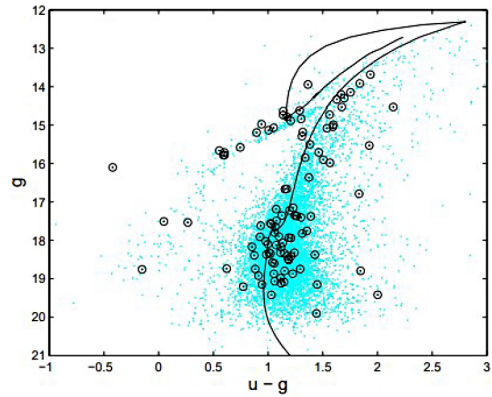


Figure 15. Location of variables on CMD. $u-g'$. The cyan color data points are the statistical average for the generated band differences as described in section 3.5.

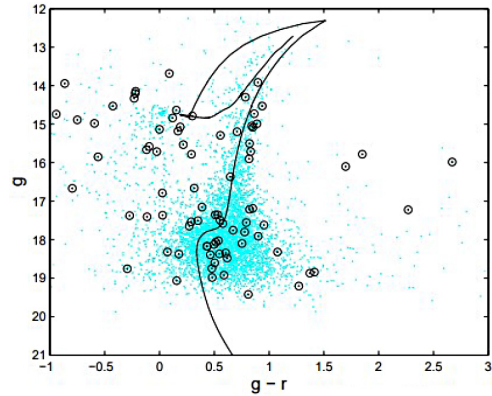


Figure 16. Location of variables on CMD. $g-r'$.

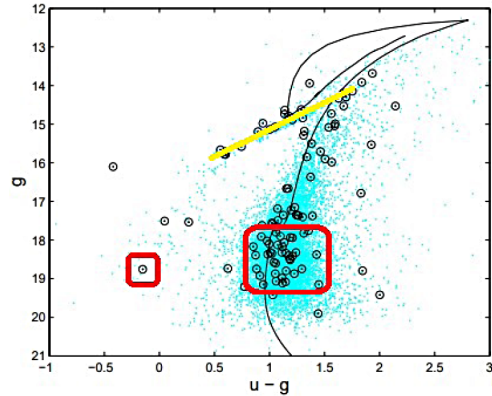


Figure 17. Groupings of variables on CMD. $u-g'$. The yellow line represents RR Lyr variables while the red box contains BY Dra variables.

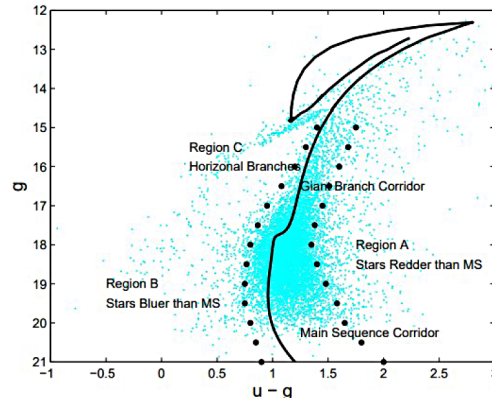


Figure 18. Example of MSGBRL and associated corridor, redder, bluer, and horizontal branch regions.

Table 4. Variables on Main Branch.

<i>ID</i> 5139 No.	<i>R.A. (J2000)</i> h m s	<i>Dec. (J2000)</i> ° ' "	<i>Period</i> (days)	<i>Type</i>
5139v-14	13 27 01.231	-47 31 49.58	0.09896	SX Phe
5139v-15	13 26 55.151	-47 31 09.49	0.04052	SX Phe
5139v-16	13 26 50.191	-47 34 03.44	0.03304	SX Phe
5139v-17	13 26 58.219	-47 34 29.86	0.03764	SX Phe
5139v-18	13 27 00.810	-47 32 41.36	0.43750	Irr/Semi
5139v-19	13 26 59.249	-47 31 38.20	0.50463	BY Dra
5139v-20	13 26 56.361	-47 31 45.61	0.36458	Irr/Semi
5139v-21	13 27 16.465	-47 33 18.10	0.30903	EA
5139v-36	13 27 12.740	-47 33 23.63	0.36921	EA
5139v-41	13 27 19.858	-47 32 17.87	0.33102	EA
5139v-42	13 27 19.999	-47 33 08.13	0.51389	Irr/Semi
5139v-45	13 27 19.732	-47 31 32.39	0.52083	Irr/Semi
5139v-47	13 27 20.947	-47 34 46.36	0.48727	RR1
5139v-48	13 27 17.820	-47 34 37.42	0.48611	Irr/Semi
5139v-49	13 27 14.128	-47 30 33.10	0.20000	BY Dra
5139v-51	13 27 13.908	-47 31 00.87	0.34060	RR0
5139v-52	13 27 16.648	-47 31 09.64	0.16703	BY Dra
5139v-53	13 27 17.108	-47 35 14.55	0.33303	Irr/Semi
5139v-55	13 27 07.985	-47 31 51.79	0.33058	Irr/Semi
5139v-56	13 27 11.793	-47 35 10.82	0.31866	BY Dra
5139v-57	13 27 19.809	-47 31 11.87	0.27778	BY Dra
5139v-58	13 27 08.163	-47 31 45.07	0.16819	Irr/Sem
5139v-59	13 27 13.788	-47 30 56.09	0.33860	RR0
5139v-62	13 27 20.284	-47 31 55.77	0.11023	BY Dra
5139v-64	13 27 16.423	-47 34 30.64	0.33064	Irr/Sem
5139v-65	13 27 15.688	-47 31 06.78	0.12426	Irr/Sem
5139v-67	13 27 21.239	-47 35 03.71	0.48958	EB
5139v-68	13 27 16.421	-47 31 07.16	0.14247	Irr/Semi
5139v-69	13 27 08.964	-47 30 18.05	0.46991	Irr/Sem
5139v-70	13 27 23.290	-47 32 51.07	0.46181	Irr/Semi
5139v-71	13 27 19.581	-47 32 07.78	0.16830	BY Dra
5139v-72	13 27 19.954	-47 30 52.41	0.56829	Irr/Sem
5139v-73	13 27 22.110	-47 31 26.10	0.14284	BY Dra
5139v-74	13 27 10.078	-47 32 02.49	0.16694	Irr/Sem
5139v-81	13 27 04.900	-47 32 27.85	0.14513	Irr/Sem
5139v-82	13 27 01.617	-47 31 00.75	0.18461	Irr/Semi
5139v-83	13 27 16.465	-47 33 18.10	0.30903	EA
5139v-84	13 26 56.922	-47 31 03.00	0.15952	Irr/Sem
5139v-101	13 27 00.303	-47 30 22.29	0.13356	Irr/Sem
5139v-104	13 26 56.589	-47 30 48.88	0.35648	Irr/Sem
5139v-106	13 26 56.430	-47 31 07.30	0.31945	EA?
5139v-108	13 26 56.537	-47 33 19.04	0.11690	Irr/Sem
5139v-110	13 26 56.741	-47 32 45.29	0.05787	Irr/Sem
5139v-112	13 27 16.465	-47 33 18.10	0.30903	Irr/Sem
5139v-116	13 27 10.511	-47 33 49.03	0.19121	Irr/Sem

were calculated and plotted. Based on preliminary results, it was determined that corridor boundaries containing approximately a $2\text{-}\sigma$ range of stars provided the best separation. The boundaries on the plots are at the $\pm 2\text{-}\sigma$ level.

Note: This is a very rough guide for initial classification purposes only. A variable residing outside but close to the MSGBRL corridor could very well belong to this GC MS. Differences in stellar color can cause a star to move position from the $u\text{'-}g\text{'}$ to $g\text{'-}r\text{'}$ diagrams. To avoid confusion, only the $g\text{'}$ vs. $u\text{'-}g\text{'}$ CMD diagrams are shown in this section.

6.1. Variable stars in the main sequence and giant branch corridor

Table 4 lists the variables that are located within the defined MS portion of the corridor for the $g\text{'}$ vs. $u\text{'-}g\text{'}$ CMD. Forty-five variables are located within this boundary just below the MS turn-off point.

Table 5. Variables redder than Main Sequence.

<i>ID</i> 5139 No.	<i>R.A. (J2000)</i> h m s	<i>Dec. (J2000)</i> ° ' "	<i>Period</i> (days)	<i>Type</i>
5139v-26	13 26 52.150	-47 31 20.52	0.46991	Irr/Sem
5139v-76	13 27 02.103	-47 35 13.15	0.15108	Irr/Sem
5139v-83	13 27 00.337	-47 31 40.88	0.14792	EA
5139v-99	13 26 56.669	-47 30 11.60	0.06223	Irr/Sem
5139v-102	13 27 00.053	-47 29 55.05	0.11868	Irr/Sem
5139v-114	13 26 57.283	-47 34 34.90	0.13371	Irr/Sem

Table 6. Stars bluer than Main Sequence.

<i>ID</i> 5139 No.	<i>R.A. (J2000)</i> h m s	<i>Dec. (J2000)</i> ° ' "	<i>Period</i> (J2000)	<i>Type</i> (days)
5139v-39	13 27 13.812	-47 30 36.45	0.24794	Irr/Sem
5139v-40	13 27 19.637	-47 31 55.75	0.33333	EW
5139v-63	13 27 18.287	-47 30 22.63	0.49769	Irr/Sem
5139v-66	13 27 17.048	-47 34 46.41	0.47222	BY Dra

Table 7. Stars on Horizontal Branch.

<i>ID</i> 5139 No.	<i>R.A. (J2000)</i> h m s	<i>Dec. (J2000)</i> ° ' "	<i>Period</i> (days)	<i>Type</i>
5139v-2	13 26 56.505	-47 30 05.77	0.3125	RR1
5139v-3	13 27 01.357	-47 31 01.96	0.65741	RR0
5139v-4	13 27 02.031	-47 30 06.80	0.33102	RR1
5139v-5	13 27 03.098	-47 30 32.83	0.32176	RR1
5139v-6	13 26 51.186	-47 31 08.57	0.37384	RR1
5139v-7	13 26 54.216	-47 30 23.15	0.47222	RR0
5139v-9	13 27 00.751	-47 34 28.71	0.58449	Irr/Semi
5139v-33	13 27 14.014	-47 30 58.22	0.34028	RR0
5139v-34	13 27 20.823	-47 33 56.82	0.48727	RR1
5139v-87	13 26 56.278	-47 30 23.24	0.1178	Irr/Sem
5139v-88	13 26 56.864	-47 32 08.87	0.06187	Irr/Sem
5139v-89	13 26 58.662	-47 32 34.72	0.11863	Irr/Sem
5139v-90	13 26 56.460	-47 34 12.50	0.09365	Irr/Sem

6.2. Stars redder than the main sequence

Variables located to the right of the MSGBRL corridor are designated as belonging to Region A, variables that are redder in color than the MS. Since the MSGBRL corridor is a rough guide to stars residing on the MS, variables that are located just outside the boundary areas could possibly belong to the MS and as such, these stars are not included in either this set or Region B.

By definition, all variables in Region A are in the extreme redder star region to the right of the MSGBRL corridor. Reviewing the phased light curves, v-26 has the characteristic shape of a BY Dra variable but it is not located on the MS and is classified as an unknown or Irr/Semiregular.

Variables v-76 and v-114 have the shape of RR Lyr but are located in the wrong region and are classified as unknown types. Variable v-99 has the general shape and period of a SX Phe. These variables are frequently referred to as pulsating blue stragglers, appearing more blue from having a higher temperature. These are located in the redder region and so cannot be classified as SX Phe and are left as unknowns. Variable v-102 seems to show some type of possible outburst activity after a short period of quiet activity and so is classified as an unknown in the list shown in Table 5.

6.3. Stars bluer than the main sequence

Variables located to the left of the MSGBRL corridor are designated as belonging to Region B, variables that are bluer than those on the MS. Following the same procedure as for Region A above, Table 6 list the variables that appear in this designated region.

This region contains EWs, CVs, white dwarfs and blue stragglers to the left of the MS turn-off point. Reviewing the phased light curves, variable v-40 has a shape that could resemble a low-mass contact eclipse and has the right period and is classified as an EW. Variables v-39 and v-63 phased light curves do not match well with any of the established templates and are classified as unknowns or Irr/Semi. Variable v-66 has a characteristic lightcurve of a BY Dra variable.

6.4. Variable stars on the horizontal branch

Thirteen variables are identified as belonging to the horizontal branch of the cluster.

This region of the cluster typically harbors RR Lyr variables. Reviewing these phased light curves, variables v-2, v-3, v-4, v-5, v-6, v-7, and v-33 have shapes matching the template of a RR Lyr. All have the correct periods and these variables have been recovered and are classified as RR Lyr. Variable v-9 looks like an EB type system, and v-34 has the phased light curve characteristic of an EW type system but its period is too long and so is likely a RR Lyr. Variables v-87, v-88, and v-90 have indications of sinusoidal activity but are classified as unknowns. Variable v-89 also has an Irr type phased light curve. The summary is shown in Table 7.

Note: For RR Lyr variables that have been designated in previous surveys, the designation is carried into the table, i.e., RR0 or RR1. For variables that have RR Lyr type light curves but have not been classified before, the table designation is RR Type.

7. Conclusions

The dataset for NGC 5139 comprises 32,072 ULTRACAM images taken over a six-day observation run in April 2011. The FOV covers a sky patch approximately 5×5 arc min², comprising two CCD chips. Using the PySIS3 software and associated processing steps resulted in 15,629, 14,950, and 9,156 light curves in the u', g', and r' SDSS filter bands, respectively. Analysis of these light curves for variable stars has produced 117 variables for the ULTRACAM data. Twenty of these were recovered from earlier surveys, leaving 97 variables that are new discoveries. A subset of the variables from ULTRACAM has been classified as belonging to classes EA, EB, EW, BY Dra, SX Phe, CV, and RR Lyr. The rest are reclassified from unknowns to general pulsating types.

Additional work would consist of follow-up observations on selected variables, especially the eclipsing binary candidates.

8. Acknowledgements

Funding for this work was provided by the University of Canterbury scholarship program. The observational data set for globular cluster NGC 5139 was provided by Associate Professor Giuseppe Bono from the University of Rome.

Many thanks to Joyce Guzik with the Los Alamos National Laboratory, Los Alamos, New Mexico, United States for reviewing the draft and especially encouraging me to publish these results.

Variable star references are contributed by Samus *et al.* (2017).

This research has made use of the SIMBAD database, operated at CDS, Strasbourg, France, 2000 (Wenger *et al.* 2000).

References

- Albrow, M. 2017, "MichaelDAlbrow/pyDIA: Initial release on github" (doi:10.5281/zenodo.268049).
- Arellano Ferro, A., Bramich, D. M., Figuera Jaimes, R., Giridhar, S., and Kuppuswamy, K. 2012, *Mon. Not. Roy. Astron. Soc.*, **420**, 1333.
- Bailey S. I. 1902, *Ann. Astron. Obs. Harvard Coll.*, **38**, 1.
- Bekki, K. and Freeman, K. C. 2003, *Mon. Not. Roy. Astron. Soc.*, **346**, L11.
- Bird, J. 2007, *Basic Engineering Mathematics*, 5th ed., Elsevier Ltd., Kidlington, Oxford, UK.
- Bono, G. 2015, private email correspondence (25 October).
- Braga V. F., *et al.* 2016, VizieR Online Data Catalog: RRLs in globulars. IV. UBVR photometry in Omega Cen (Braga+, 2016 *Astron. J.*, **152**, 170).
- Braga V. F., *et al.* 2018, VizieR Online Data Catalog: RRLs in globulars. V. ω Centauri NIR photometry (Braga+, 2018 *Astron. J.*, **155**, 137).
- Bramich D. M. 2008, *Mon. Not. Roy. Astron. Soc.*, **386**, L77.
- Bramich, D. M., Figuera J. R., Giridhar, S., Arellano Ferro, A. 2011, *Mon. Not. Roy. Astron. Soc.*, **413**, 1275.
- Carpenter, J. M., Hillenbrand, L. A., Skrutskie, M. F., and Meyer, M. R. 2002, *Astron. J.*, **124**, 1001.
- Chonis, T. S., and Gaskell, C. M. 2008, *Astron. J.*, **135**, 264.
- Clement, C., 2017, in Wide-Field Variability Surveys: A 21st Century Perspective, eds. M. Catelan, W. Gieren, EPJ Web Conf., 152, 01021 (<http://www.astro.utoronto.ca/~cclement/cat/listngc.html>).
- Corwin, T. M., Sumarel, A. N., Pritzl, B. J., Smith, H. A., Catelan, M., Sweigart, A. V., and Stetson, P. B. 2006, *Astron. J.*, **132**, 1014.
- Covey, K. R., *et al.* 2007, *Astron. J.*, **134**, 2398.
- Dhillon, V. S., *et al.* 2007, *Mon. Not. Roy. Astron. Soc.*, **378**, 825.
- Dickens, R. J., Feast, M. W., and Lloyd Evans, T. 1972, *Mon. Not. Roy. Astron. Soc.*, **159**, 337.
- Fourcade, C. R., Laborde, J. R. and Yurquina, E. 1978, *Inf. Bull. Var. Stars*, No. 1380, 1.
- Fukugita, M., Ichikawa, T., Gunn, J. E., Doi, M., Shimasaku, K., and Schneider, D. P. 1996, *Astron. J.*, **111**, 1748.
- Harris, W. E. 1996, *Astron. J.*, **112**, 1487.
- Jorgensen, H. E., and Hansen, L. 1984, *Astron. Astrophys.*, **133**, 165.
- Kains, N., Bramich, D. M., Figuera Jaimes, R., Arellano Ferro, A., Giridhar, S., and Kuppuswamy, K. 2012, *Astron. Astrophys.*, **548A**, 92.
- Kovács, G., Bakos, G., and Noyes, R. W. 2005, *Mon. Not. Roy. Astron. Soc.*, **356**, 557.

- Kovács, G., Zucker, S., and Mazeh, T. 2002, *Astron. Astrophys.*, **391**, 369.
- Magurno, D., *et al.* 2018, *Astrophys. J.*, **864**, 57.
- Martin, W. C. 1938, *Ann. Sterrewacht Leiden*, **17**, B1.
- Mortier, A., Faria, J. P., Correia, C. M., Santerne, A., and Santos, N. C. 2015, *Astron. Astrophys.*, **573A**, 101.
- Mukherjee, K., Anthony-Twarog, B. J., and Twarog, B. A. 1992, *Publ. Astron. Soc. Pacific*, **104**, 561.
- Navarrete, C., Catelan, M., Contreras Ramos, R., Alonso-García, J., Gran, F., Dékány, I., and Minniti, D. 2017, *Astron. Astrophys.*, **604A**, 120.
- Navarrete, C., *et al.* 2015, *Astron. Astrophys.*, **577A**, 99.
- Niss, B., Jorgensen, H. E., and Laustsen, S. 1978, *Astron. Astrophys., Suppl. Ser.*, **32**, 387.
- Plavchan, P., Jura, M., Kirkpatrick, J. D., Cutri, R. M., and Gallagher, S. C. 2008, *Astrophys. J., Suppl. Ser.*, **175**, 191.
- Rice, T. S., Wolk, S. J., and Aspin, C. 2012, *Astrophys. J.*, **755**, 65.
- Samus, N. N., Kazarovets, E. V., Durlevich, O. V., Kireeva, N. N., and Pastukhova, E. N. 2017, *Astron. Rep.*, **61**, 80 (*General Catalogue of Variable Stars: version GCVS 5.1*, <http://www.sai.msu.su/groups/cluster/gcvs/gcvs>).
- Savitzky, A., and Golay, M. J. E. 1964, *Anal. Chem.*, **36**, 1627.
- Sawyer Hogg, H. 1973, *Publ. David Dunlap Obs.*, **3**, 6.
- Scargle, J. D. 1982, *Astrophys. J.*, **263**, 835.
- Stellingwerf, R. F. 1978, *Astrophys. J.*, **224**, 953.
- Stetson, P. B. 2015, Photometric standard fields, Canadian Astronomy Data Centre. Canadian Astronomy Data Centre.¹
- Strader, J., Everitt, H. O., and Danford, S. 2002, *Mon. Not. Roy. Astron. Soc.*, **335**, 621.
- van Dokkum, P. 2001, *Publ. Astron. Soc. Pacific*, **113**, 1420.
- Walker, D. 2016, *A High Cadence Photometric Survey of Five Southern Hemisphere Milky Way Globular Clusters*, doctoral dissertation, University of Canterbury, Christchurch, New Zealand.
- Wenger, M., *et al.* 2000, *Astron. Astrophys., Suppl. Ser.*, **143**, 9.

¹ Stetson (2015), (<http://www4.cadc-ccda.hia-ihp.nrc-cnrc.gc.ca/en/community/STETSON/standards/>)

Appendix A: Master catalog of detected variable stars.

Table A1. Master catalog.

Variable ID	R.A. (J2000)			Dec. (J2000)			Period (days)	u'	g'	Mag r'	Confidence Level	Variable Class	Recovered Survey	Recovered Class
	h	m	s	°	'	"								
5139v-1	13	26	56.269	-47	31	47.67	0.36574	15.90	14.15	14.36	EH	RR0	Yes	RR0
5139v-2	13	26	56.505	-47	30	05.77	0.31250	15.91	14.62	15.81	H	RR0	Yes	RR1
5139v-3	13	27	01.357	-47	31	01.96	0.65741	15.77	14.63	—	H	RR0	Yes	RR0
5139v-4	13	27	02.031	-47	30	06.80	0.33102	15.88	14.74	15.68	EH	RR0	Yes	RR1
5139v-5	13	27	03.098	-47	30	32.83	0.32176	15.96	14.79	—	M	RR1	Yes	RR1
5139v-6	13	26	51.186	-47	31	08.57	0.37384	16.09	14.89	15.64	H	RR0	Yes	RR1
5139v-7	13	26	54.216	-47	30	23.15	0.47222	15.92	14.98	—	H	RR0	Yes	RR0
5139v-8	13	27	00.962	-47	31	24.56	0.18539	16.88	15.50	—	M	Irr/Semi	No	NA
5139v-9	13	27	00.751	-47	34	28.71	0.58449	16.31	15.71	15.74	L	Irr/Semi	No	NA
5139v-10	13	27	00.788	-47	31	57.91	0.56250	16.38	15.78	—	L	EA	No	NA
5139v-11	13	26	56.273	-47	30	50.05	0.38079	—	16.10	—	EH	RR1	Yes	RR1
5139v-12	13	27	00.886	-47	32	48.18	0.65857	17.74	16.36	15.72	M	EA	No	NA
5139v-13	13	26	58.684	-47	29	50.82	0.04140	17.82	16.67	—	H	SX Phe	Yes	SX Phe
5139v-14	13	27	01.231	-47	31	49.58	0.09896	18.38	17.15	16.77	H	SX Phe	Yes	SX Phe
5139v-15	13	26	55.151	-47	31	09.49	0.04052	18.63	17.37	—	H	SX Phe	No	NA
5139v-16	13	26	50.191	-47	34	03.44	0.03304	18.71	17.41	—	H	SX Phe	Yes	SX Phe
5139v-17	13	26	58.219	-47	34	29.86	0.03764	18.57	17.49	16.94	H	SX Phe	No	NA
5139v-18	13	27	00.810	-47	32	41.36	0.43750	18.61	17.58	17	M	Irr/Semi	No	NA
5139v-19	13	26	59.249	-47	31	38.20	0.50463	19.14	17.82	—	H	BY Dra	No	NA
5139v-20	13	26	56.361	-47	31	45.61	0.36458	19.12	17.93	—	H	Irr/Semi	No	NA
5139v-21	13	27	00.636	-47	33	13.04	0.39120	19.20	18.13	17.63	M	EA	No	NA
5139v-22	13	26	53.172	-47	34	22.95	0.11088	19.56	18.32	—	H	BY Dra	No	NA
5139v-23	13	26	57.278	-47	32	34.48	0.33333	19.49	18.34	—	H	EA	No	NA
5139v-24	13	26	58.270	-47	34	52.76	0.66088	19.62	18.41	—	M	EA	No	NA
5139v-25	13	26	57.819	-47	35	33.01	0.57755	19.70	18.51	—	L	EA	No	NA
5139v-26	13	26	52.150	-47	31	20.52	0.46991	20.64	18.79	—	M	Irr/Semi	No	NA
5139v-27	13	27	06.428	-47	30	03.29	0.18615	—	18.84	—	H	Irr/Semi	No	NA
5139v-28	13	26	53.910	-47	34	17.99	0.09954	—	19.66	—	H	SX Phe	No	NA
5139v-29	13	27	15.879	-47	31	10.14	0.42245	15.87	14.20	14.42	H	RR1	Yes	NA
5139v-30	13	27	16.465	-47	33	18.10	0.30903	15.96	14.33	14.56	H	RR1	Yes	NA
5139v-31	13	27	22.097	-47	30	12.66	0.69213	16.20	14.53	14.95	EH	RR0	Yes	RR0
5139v-32	13	27	11.551	-47	35	02.68	0.47338	16.50	15.18	15.01	EH	EA	Yes	EA
5139v-33	13	27	14.014	-47	30	58.22	0.34028	16.09	15.19	14.49	EH	RR0	No	NA
5139v-34	13	27	20.823	-47	33	56.82	0.48727	16.33	15.58	15.67	H	RR1	No	NA
5139v-35	13	27	20.198	-47	31	49.75	0.30002	17.83	16.66	16.35	EH	EA	Yes	EA
5139v-36	13	27	12.740	-47	33	23.63	0.36921	18.26	17.19	16.34	H	EA	No	NA
5139v-37	13	27	13.757	-47	32	24.92	0.13466	—	17.21	16.39	H	EW	Yes	EW
5139v-38	13	27	22.950	-47	32	18.85	0.12032	18.61	17.36	16.85	M	EW	Yes	EW
5139v-39	13	27	13.812	-47	30	36.45	0.24794	17.56	17.51	17.16	M	Irr/Semi	No	NA
5139v-40	13	27	19.637	-47	31	55.75	0.33333	17.80	17.54	17.25	H	EW	No	NA
5139v-41	13	27	19.858	-47	32	17.87	0.33102	18.58	17.56	16.76	M	EA	No	NA
5139v-42	13	27	19.999	-47	33	08.13	0.51389	18.55	17.62	16.67	H	Irr/Semi	No	NA
5139v-43	—	—	—	—	—	—	0.12000	17.74	17.08	19.10	H	Irr/Semi	No	NA
5139v-44	13	27	15.141	-47	31	21.80	0.16464	18.86	17.80	17.02	H	EW	No	NA
5139v-45	13	27	19.732	-47	31	32.39	0.52083	19.00	17.90	—	L	Irr/Semi	No	NA
5139v-46	13	27	12.715	-47	32	55.32	0.32870	18.84	17.91	17.01	H	Irr/Semi	No	NA
5139v-47	13	27	20.947	-47	34	46.36	0.48727	19.15	17.94	—	H	RR1	No	NA
5139v-48	13	27	17.820	-47	34	37.42	0.48611	19.00	18.03	17.49	H	Irr/Semi	No	NA
5139v-49	13	27	14.128	-47	30	33.10	0.20000	19.20	18.07	17.55	M	BY Dra	No	NA
5139v-50	13	27	17.786	-47	30	59.77	0.14167	—	18.09	—	M	BY Dra	No	NA
5139v-51	13	27	13.908	-47	31	00.87	0.34060	19.10	18.10	17.35	EH	RR0	No	NA
5139v-52	13	27	16.648	-47	31	09.64	0.16703	19.02	18.17	17.74	H	BY Dra	No	NA
5139v-53	13	27	17.108	-47	35	14.55	0.33303	19.29	18.18	17.74	H	Irr/Semi	No	NA
5139v-54	13	27	12.941	-47	30	31.47	0.16826	—	18.28	—	M	Irr/Semi	No	NA
5139v-55	13	27	07.985	-47	31	51.79	0.33058	19.33	18.32	17.24	H	Irr/Semi	No	NA
5139v-56	13	27	11.793	-47	35	10.82	0.31866	19.37	18.35	17.74	H	BY Dra	No	NA
5139v-57	13	27	19.809	-47	31	11.87	0.27778	19.35	18.37	17.83	H	BY Dra	No	NA
5139v-58	13	27	08.163	-47	31	45.07	0.16819	19.27	18.39	17.93	H	Irr/Semi	No	NA
5139v-59	13	27	13.788	-47	30	56.09	0.33860	19.66	18.48	17.86	EH	RR0	No	NA
5139v-60	13	27	14.521	-47	30	57.36	0.33824	19.62	18.58	—	H	RR0	Yes	RR0
5139v-61	—	—	—	—	—	—	0.33824	19.62	18.58	—	H	Irr/Semi	No	NA
5139v-62	13	27	20.284	-47	31	55.77	0.11023	19.66	18.60	18.1	H	BY Dra	No	NA
5139v-63	13	27	18.287	-47	30	22.63	0.49769	19.36	18.74	—	M	Irr/Semi	No	NA

Table continued on next page

Table A1. Master catalogue, cont.

Variable ID	R.A. (J2000)			Dec. (J2000)			Period (days)	u'	g'	Mag r'	Confidence Level	Variable Class	Recovered Survey	Recovered Class
	h	m	s	°	'	"								
5139v-64	13	27	16.423	-47	34	30.64	0.33064	19.63	18.75	18.27	L	Irr/Semi	No	NA
5139v-65	13	27	15.688	-47	31	06.78	0.12426	20.04	18.75	—	H	Irr/Semi	No	NA
5139v-66	13	27	17.048	-47	34	46.41	0.47222	18.60	18.76	19.05	L	BY Dra	No	NA
5139v-67	13	27	21.239	-47	35	03.71	0.48958	19.95	18.80	—	H	EB	No	NA
5139v-68	13	27	16.421	-47	31	07.16	0.14247	20.10	18.87	—	M	Irr/Semi	No	NA
5139v-69	13	27	08.964	-47	30	18.05	0.46991	19.92	18.87	17.5	L	Irr/Semi	No	NA
5139v-70	13	27	23.290	-47	32	51.07	0.46181	19.83	18.92	18.33	H	Irr/Semi	No	NA
5139v-71	13	27	19.581	-47	32	07.78	0.16830	20.10	18.98	18.5	H	BY Dra	No	NA
5139v-72	13	27	19.954	-47	30	52.41	0.56829	20.13	19.07	18.91	M	Irr/Semi	No	NA
5139v-73	13	27	22.110	-47	31	26.10	0.14284	20.24	19.12	—	H	BY Dra	No	NA
5139v-74	13	27	10.078	-47	32	02.49	0.16694	20.45	19.42	18.61	H	Irr/Semi	No	NA
5139v-75	13	27	01.120	-47	31	05.83	0.16212	—	—	13.51	M	Irr/Semi	No	NA
5139v-76	13	27	02.103	-47	35	13.15	0.15108	16.67	14.53	13.59	H	Irr/Semi	No	NA
5139v-77	13	27	01.571	-47	31	07.12	0.21840	16.37	15.78	13.93	H	RR0	No	NA
5139v-78	—	—	—	—	—	—	0.16308	14.61	15.49	16.76	H	Irr/Semi	No	NA
5139v-79	13	26	59.358	-47	35	26.63	0.28026	16.60	15.29	14.73	H	Irr/Semi	No	NA
5139v-80	13	26	50.531	-47	35	19.36	0.21150	—	—	16.41	H	Irr/Semi	No	NA
5139v-81	13	27	04.900	-47	32	27.85	0.14513	18.48	17.35	16.82	L	Irr/Semi	No	NA
5139v-82	13	27	01.617	-47	31	00.75	0.18461	—	—	17.38	H	Irr/Semi	No	NA
5139v-83	13	27	00.337	-47	31	40.88	0.14792	—	—	18.2	M	EA	No	NA
5139v-84	13	26	56.922	-47	31	03.00	0.15952	19.43	18.32	18.25	M	Irr/Semi	No	NA
5139v-85	13	26	56.656	-47	29	51.98	0.05888	15.62	13.68	—	M	Irr/Semi	No	NA
5139v-86	13	26	56.551	-47	30	54.78	0.09482	15.75	13.92	—	M	Irr/Semi	No	NA
5139v-87	13	26	56.278	-47	30	23.24	0.11780	16.12	15.07	—	L	Irr/Semi	No	NA
5139v-88	13	26	56.864	-47	32	08.87	0.06187	16.14	15.13	15.13	L	Irr/Semi	No	NA
5139v-89	13	26	58.662	-47	32	34.72	0.11863	16.14	14.84	14.72	L	Irr/Semi	No	NA
5139v-90	13	26	56.460	-47	34	12.50	0.09365	16.22	15.66	15.78	M	Irr/Semi	No	NA
5139v-91	13	26	58.212	-47	31	22.12	0.13339	16.29	14.73	—	M	Irr/Semi	No	NA
5139v-92	13	27	04.258	-47	30	28.90	0.13393	16.36	—	16.37	H	Irr/Semi	No	NA
5139v-93	13	26	56.756	-47	32	35.74	0.54977	16.59	14.99	14.1	L	Irr/Semi	No	NA
5139v-94	13	26	56.473	-47	33	21.68	0.09410	16.62	15.08	14.23	M	Irr/Semi	No	NA
5139v-95	13	26	56.799	-47	31	40.88	0.04438	16.64	15.04	—	L	Irr/Semi	No	NA
5139v-96	13	27	00.845	-47	30	14.24	0.09660	17.09	—	15.13	M	Irr/Semi	No	NA
5139v-97	13	26	56.418	-47	33	41.34	0.26620	17.17	15.71	14.88	M	Irr/Semi	No	NA
5139v-98	13	26	56.458	-47	34	05.44	0.09375	17.41	15.90	15.08	L	Irr/Semi	No	NA
5139v-99	13	26	56.669	-47	30	11.60	0.06223	17.46	15.53	—	M	Irr/Semi	No	NA
5139v-100	13	27	02.386	-47	31	26.65	0.13283	17.55	15.98	13.31	H	Irr/Semi	No	NA
5139v-101	13	27	00.303	-47	30	22.29	0.13356	18.60	17.36	—	M	Irr/Semi	No	NA
5139v-102	13	27	00.053	-47	29	55.05	0.11868	18.62	16.79	—	M	Irr/Semi	No	NA
5139v-103	13	26	55.615	-47	30	06.55	0.10621	18.73	—	16.88	M	Irr/Semi	No	NA
5139v-104	13	26	56.589	-47	30	48.88	0.35648	18.77	17.38	—	L	Irr/Semi	No	NA
5139v-105	13	27	00.636	-47	33	58.03	0.06008	19.50	—	—	L	Irr/Semi	No	NA
5139v-106	13	26	56.430	-47	31	07.30	0.31945	19.58	18.40	—	M	EA?	No	NA
5139v-107	13	27	00.608	-47	31	13.27	0.10728	20.03	—	—	M	Irr/Semi	No	NA
5139v-108	13	26	56.537	-47	33	19.04	0.11690	20.10	19.15	—	L	Irr/Semi	No	NA
5139v-109	13	26	55.795	-47	29	56.66	0.13407	20.12	—	—	L	Irr/Semi	No	NA
5139v-110	13	26	56.741	-47	32	45.29	0.05787	20.23	19.08	—	L	Irr/Semi	No	NA
5139v-111	13	26	56.514	-47	32	42.52	0.13277	20.38	—	—	M	Irr/Semi	No	NA
5139v-112	13	26	58.523	-47	32	37.24	0.13354	20.60	19.15	—	M	Irr/Semi	No	NA
5139v-113	13	26	53.782	-47	35	28.42	0.13320	21.34	19.90	—	H	Irr/Semi	No	NA
5139v-114	13	26	57.283	-47	34	34.90	0.13371	21.42	19.42	—	L	Irr/Semi	No	NA
5139v-115	13	27	21.678	-47	32	08.55	0.17780	15.31	13.94	14.81	M	Irr/Semi	No	NA
5139v-116	13	27	10.511	-47	33	49.03	0.19121	18.42	17.22	14.95	L	Irr/Semi	No	NA
5139v-117	13	27	09.921	-47	32	48.49	0.18986	19.98	19.21	17.93	M	Irr/Semi	No	NA

Appendix B: Master catalog of light curves of variable stars.

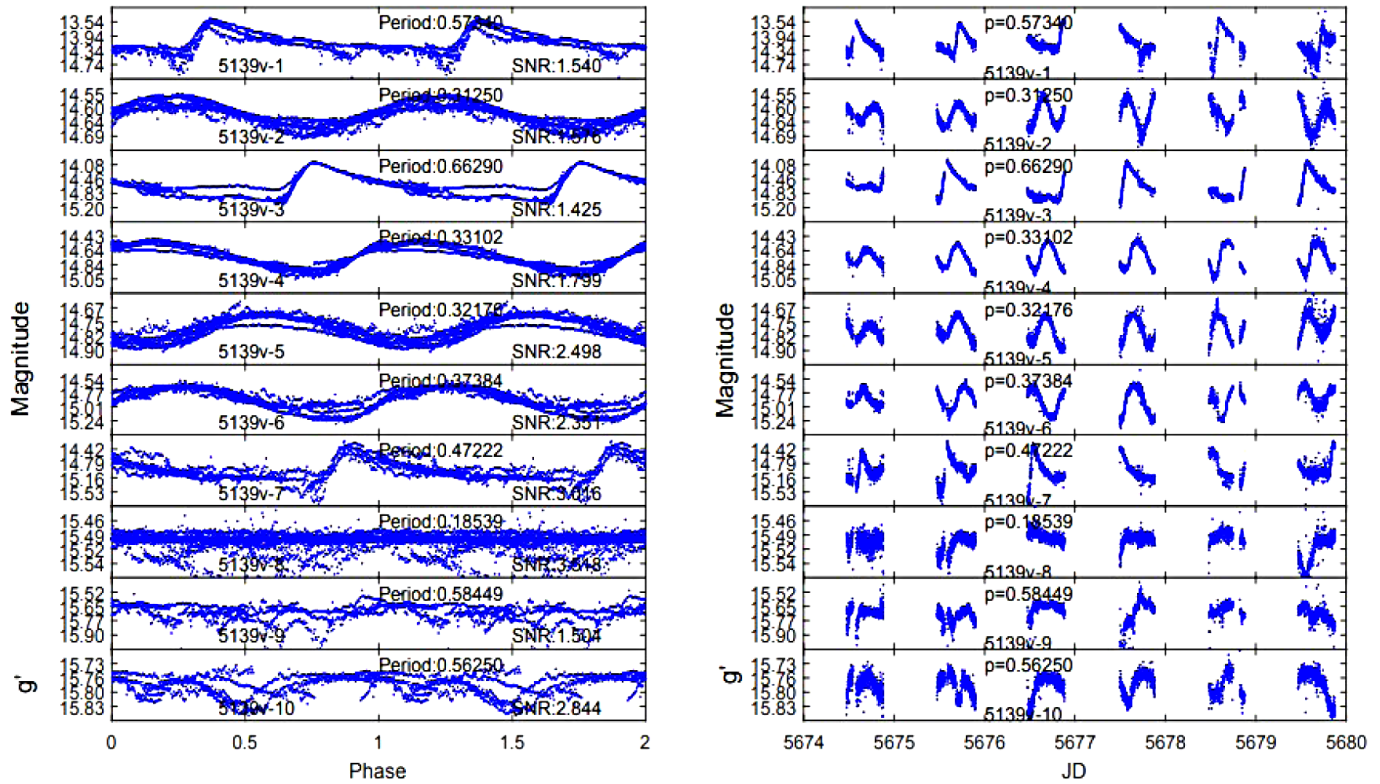


Figure B1. Phase and light curves for g' primary band for variables 5139v- 1–10. Left panel: phased light curves. Right panel: time series light curves.

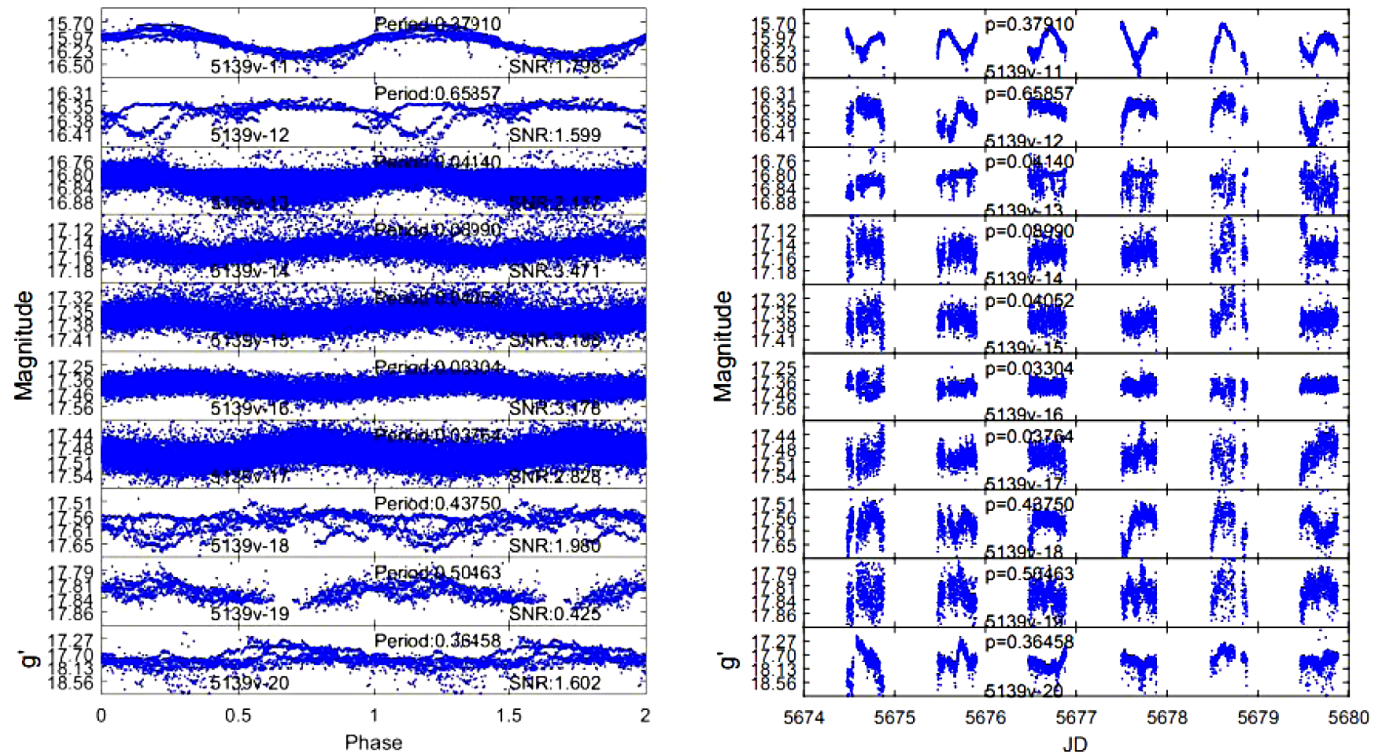
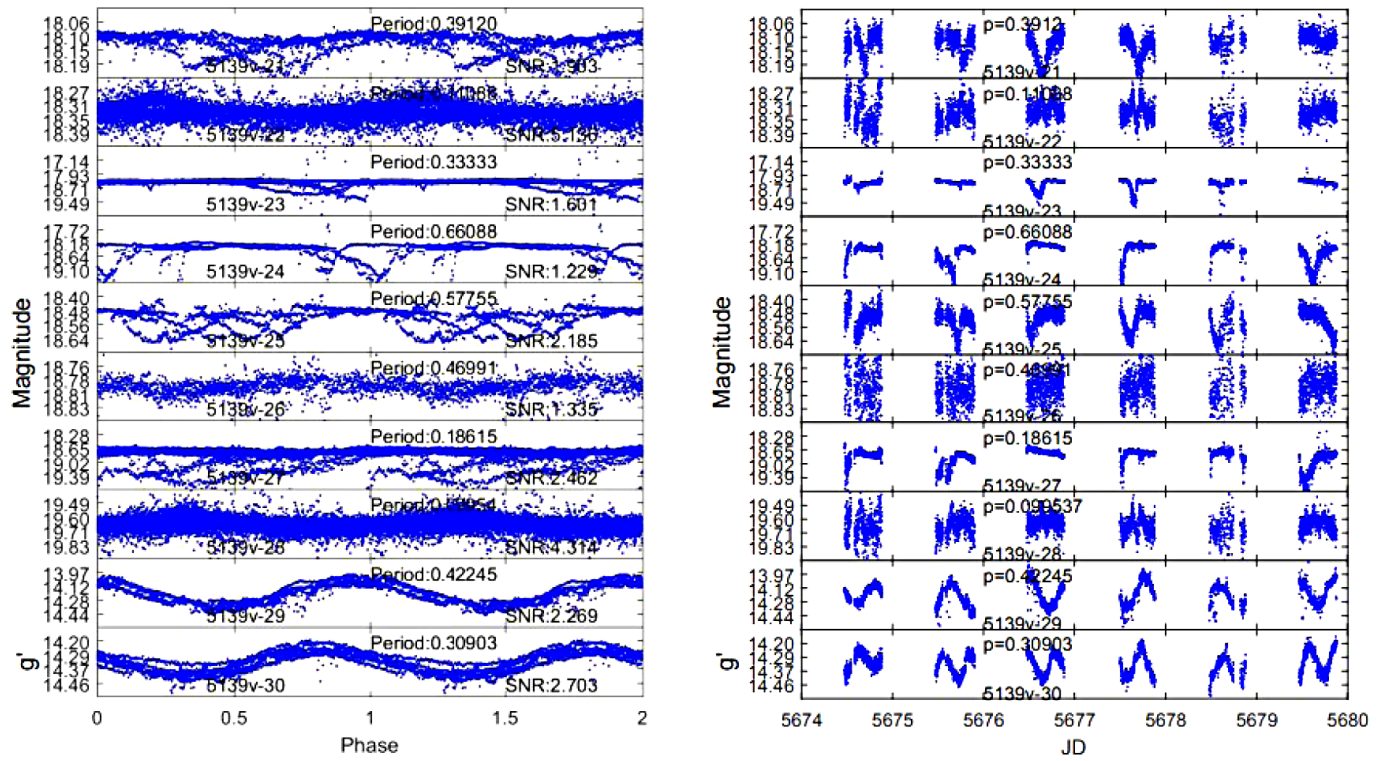
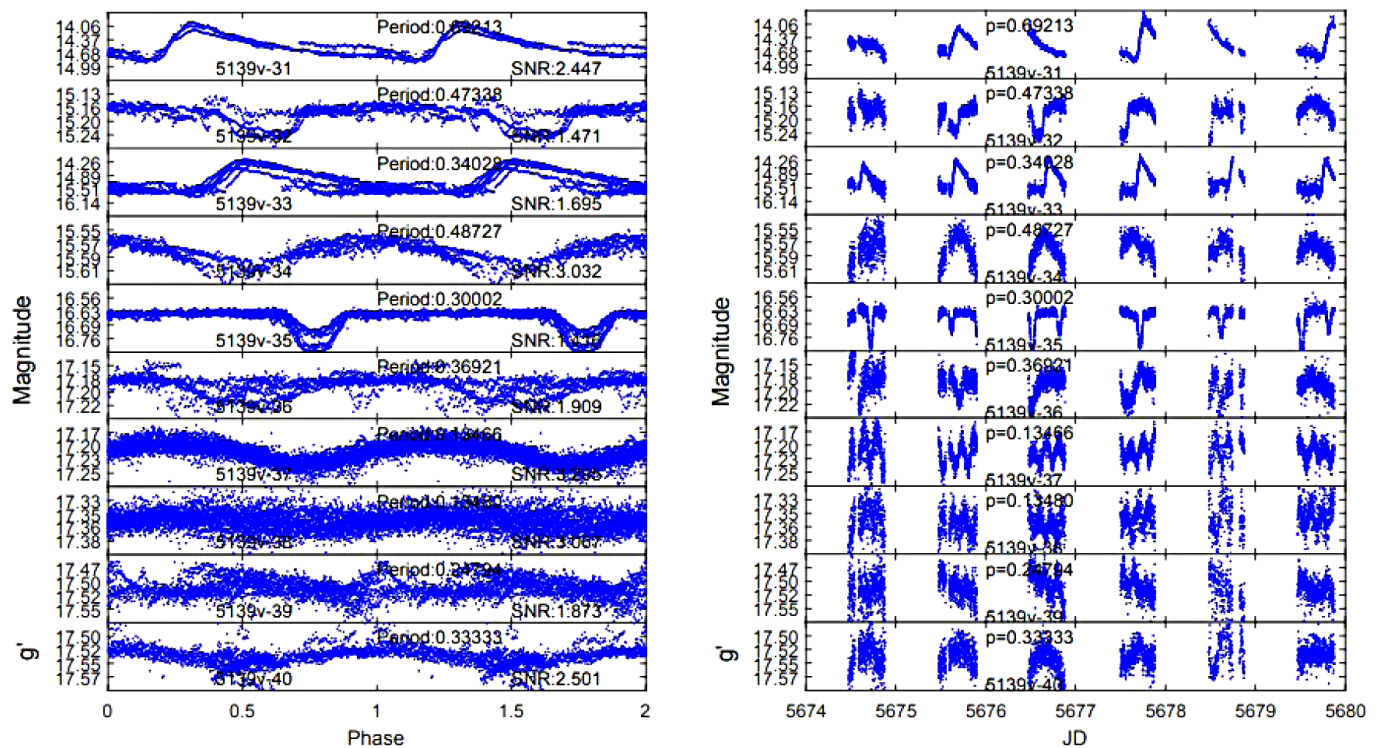


Figure B2. Phase and light curves for g' primary band for variables 5139v- 11–20. Left panel: phased light curves. Right panel: time series light curves.

Figure B3. Phase and light curves for g' primary band for variables 5139v- 21–30. Left panel: phased light curves. Right panel: time series light curves.Figure B4. Phase and light curves for g' primary band for variables 5139v- 31–40. Left panel: phased light curves. Right panel: time series light curves.

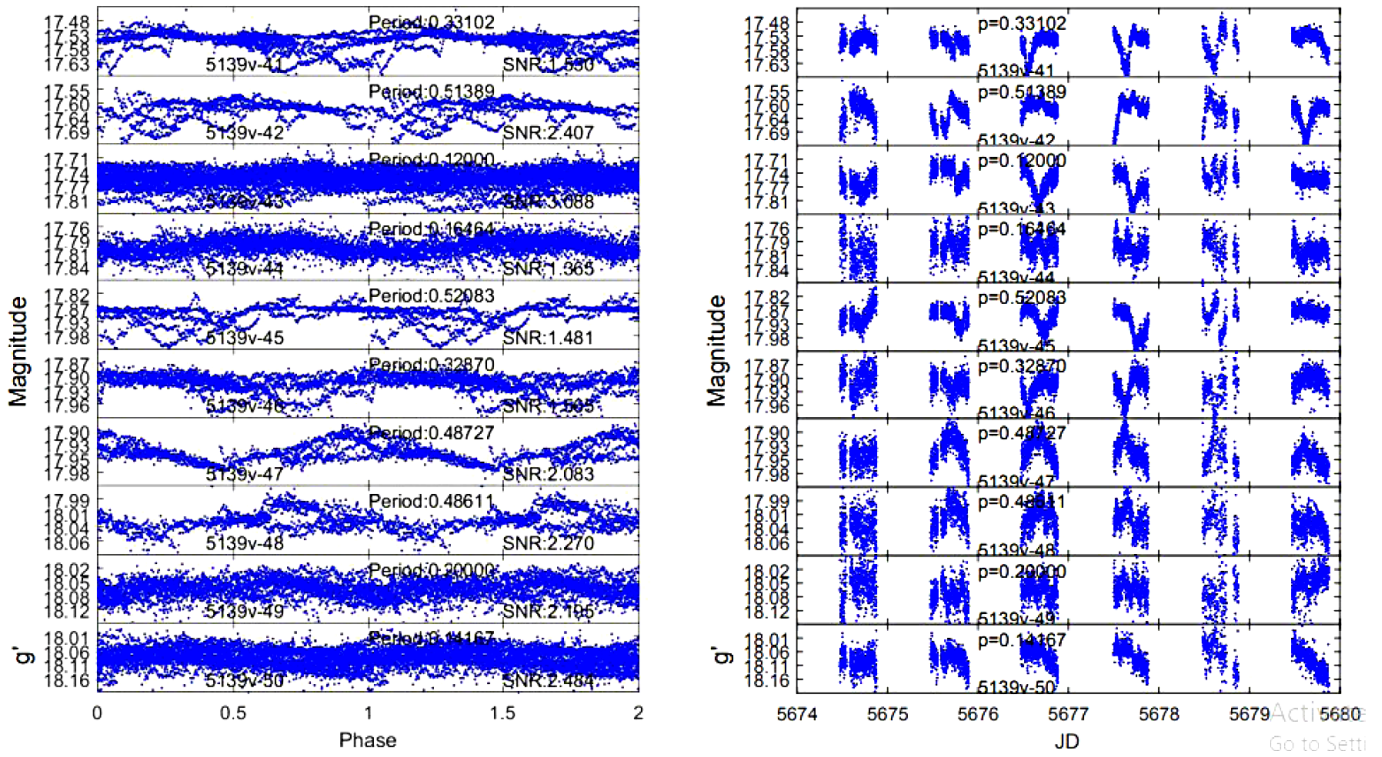


Figure B5. Phase and light curves for g' primary band for variables 5139v- 41–50. Left panel: phased light curves. Right panel: time series light curves.

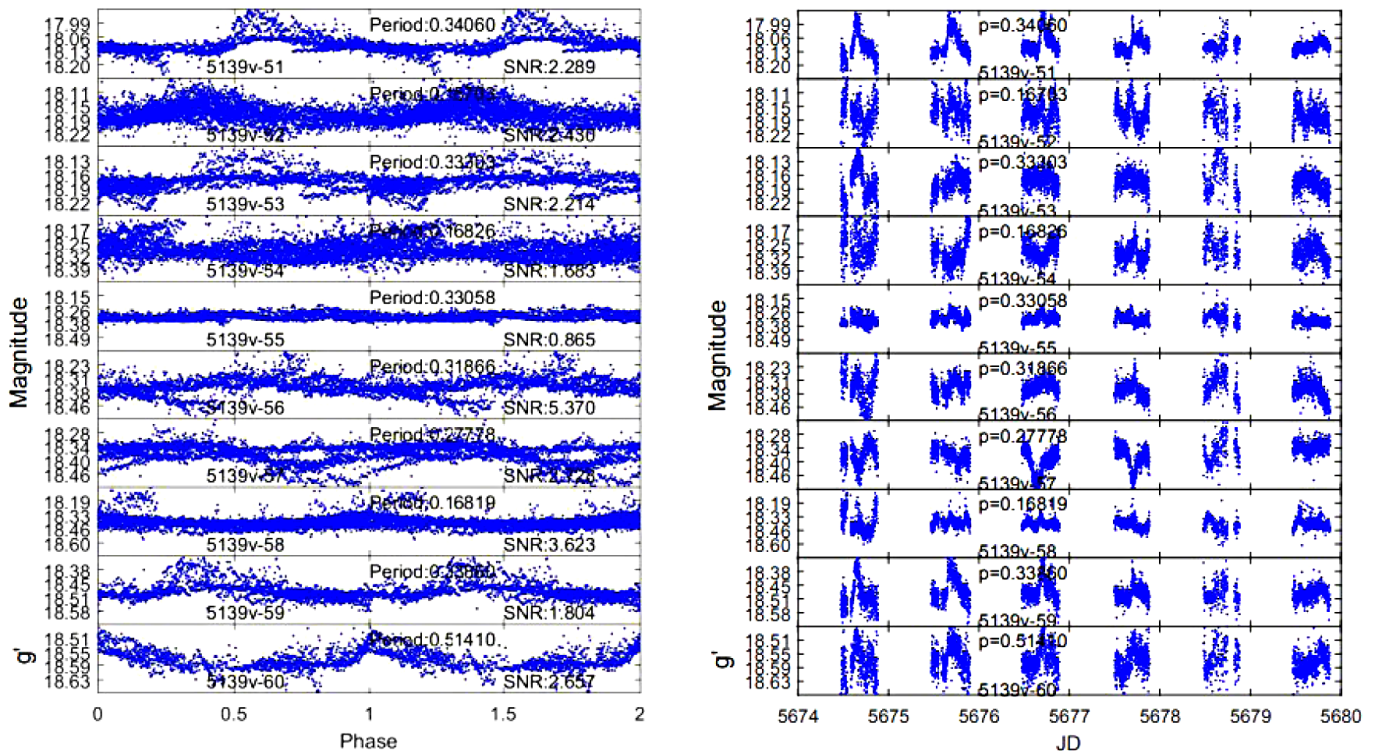


Figure B6. Phase and light curves for g' primary band for variables 5139v- 51–60. Left panel: phased light curves. Right panel: time series light curves.

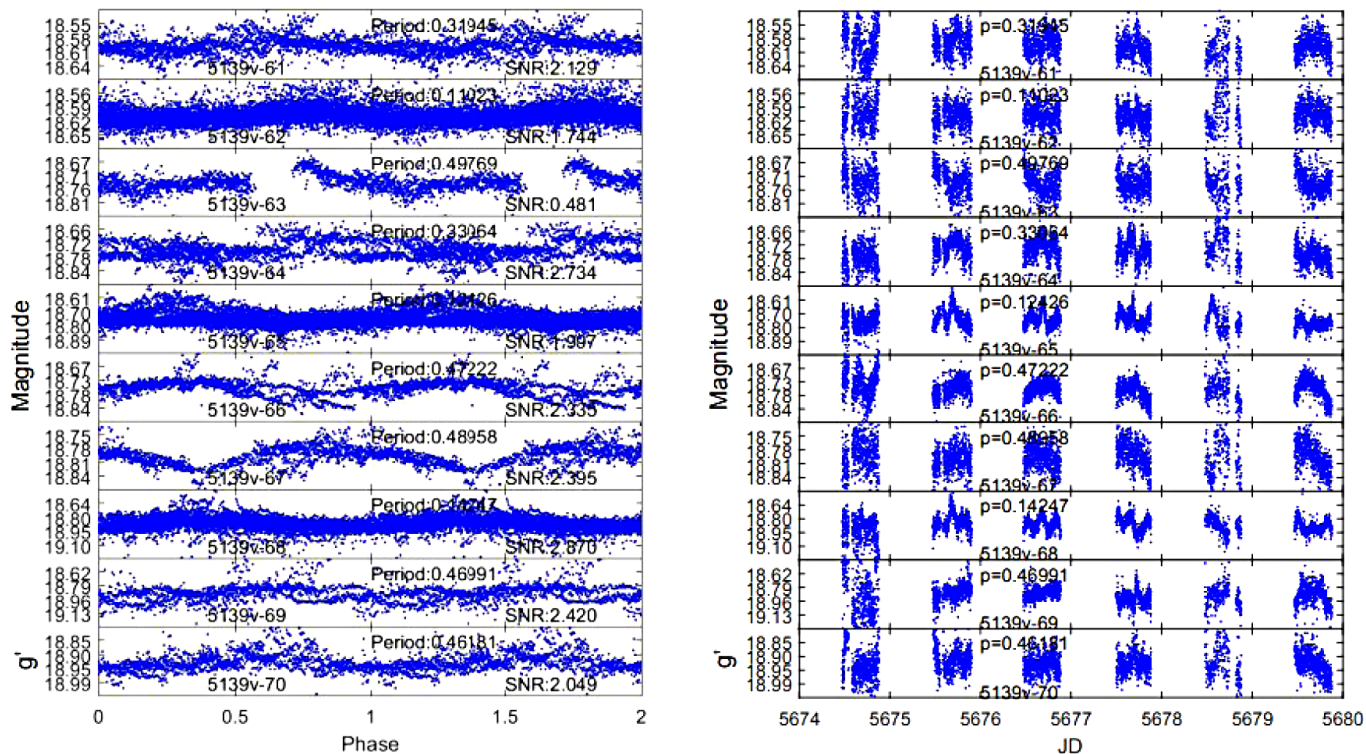


Figure B7. Phase and light curves for g' primary band for variables 5139v- 61–70. Left panel: phased light curves. Right panel: time series light curves.

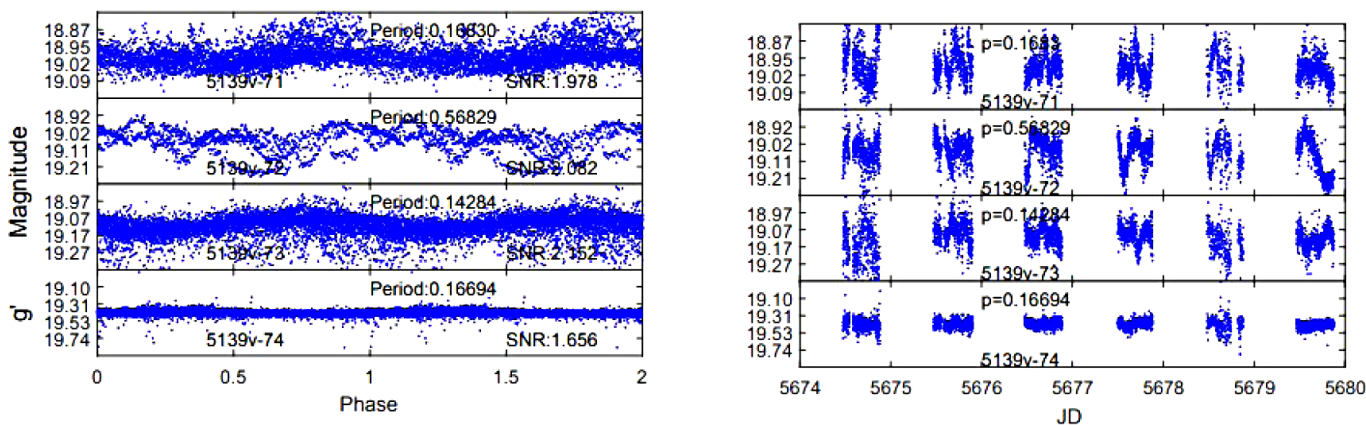


Figure B8. Phase and light curves for g' primary band for variables 5139v- 71–74. Left panel: phased light curves. Right panel: time series light curves.

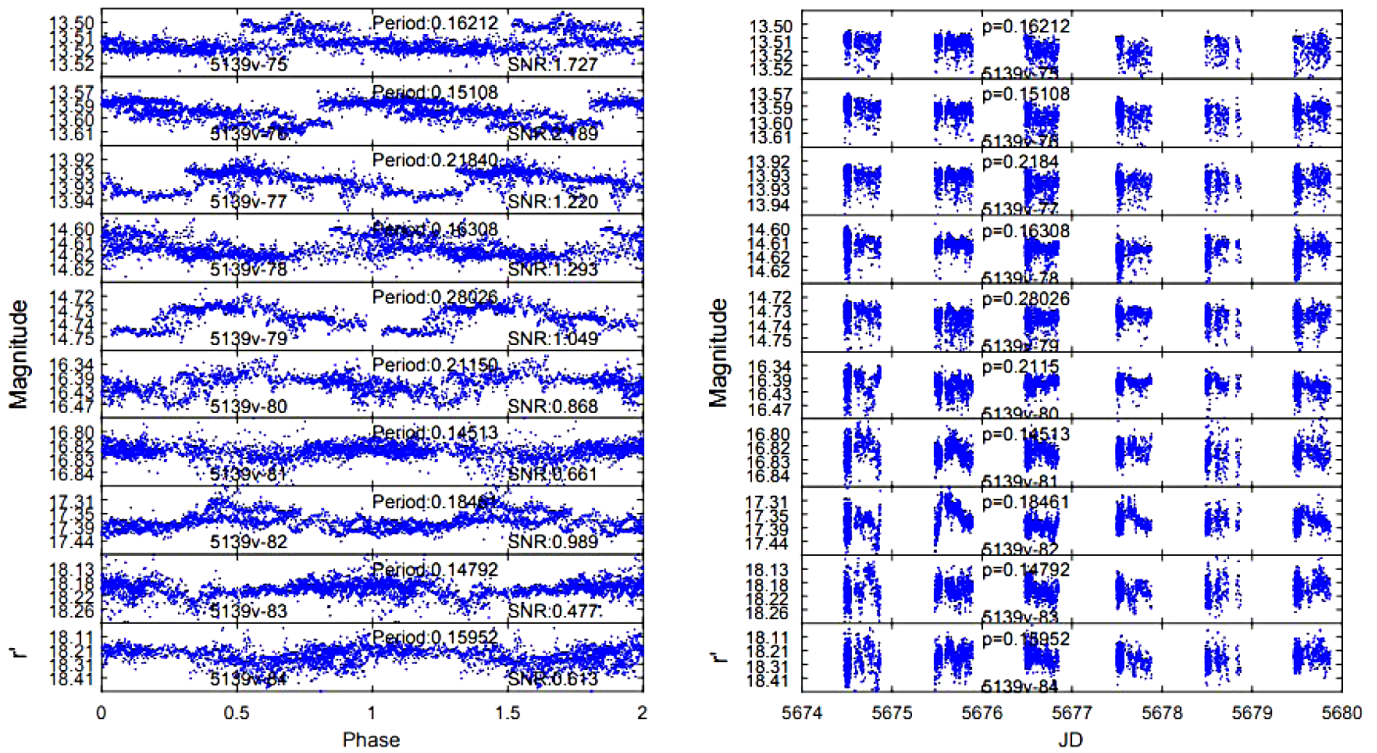


Figure B9. Phase and light curves for r' primary band for variables 5139v- 75–84. Left panel: phased light curves. Right panel: time series light curves.

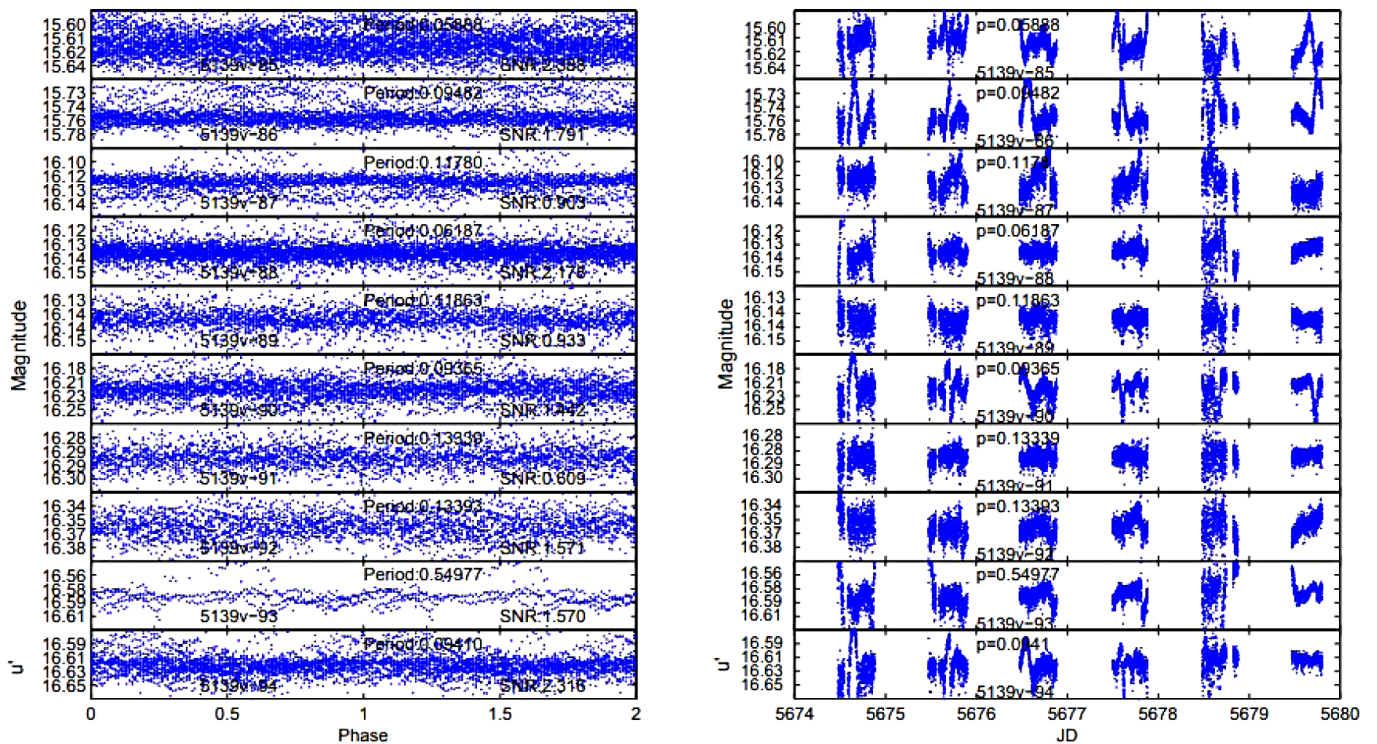


Figure B10. Phase and light curves for u' primary band for variables 5139v- 85–94. Left panel: phased light curves. Right panel: time series light curves.

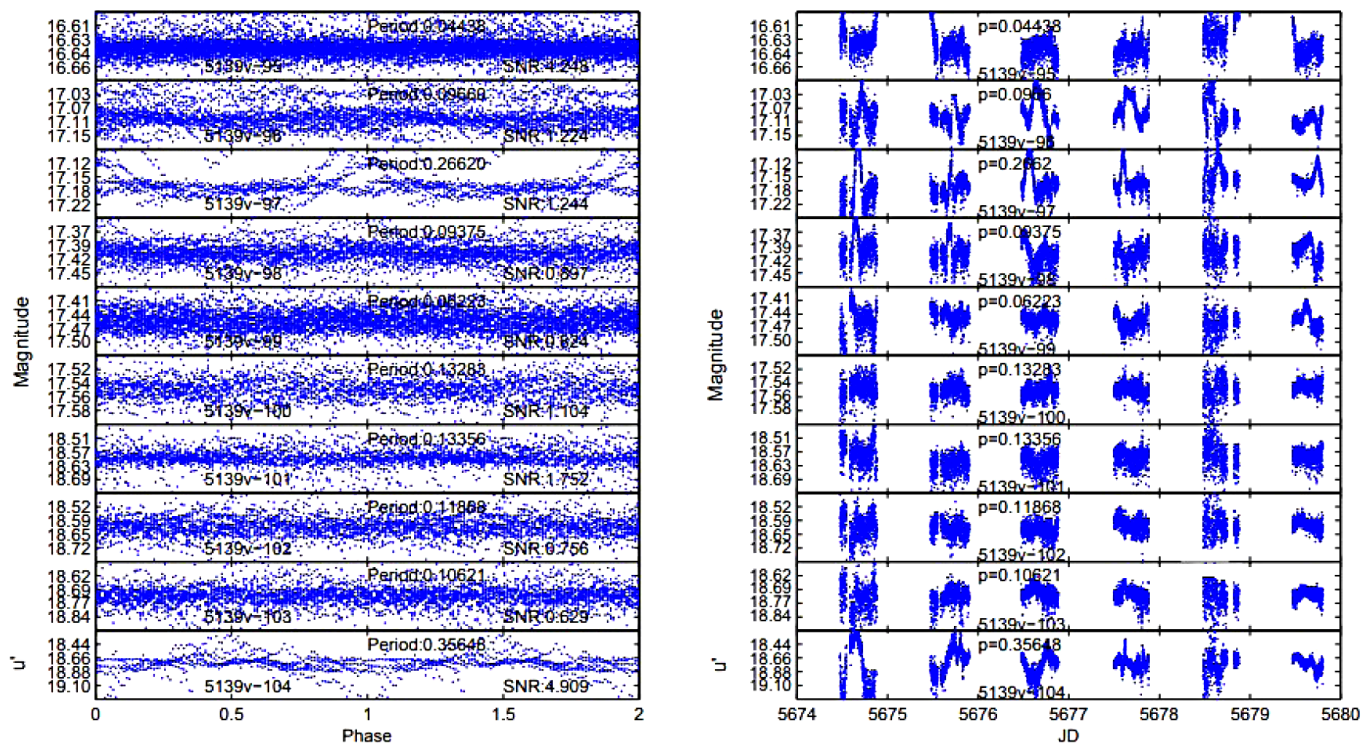


Figure B11. Phase and light curves for u' primary band for variables 5139v- 95–104. Left panel: phased light curves. Right panel: time series light curves.

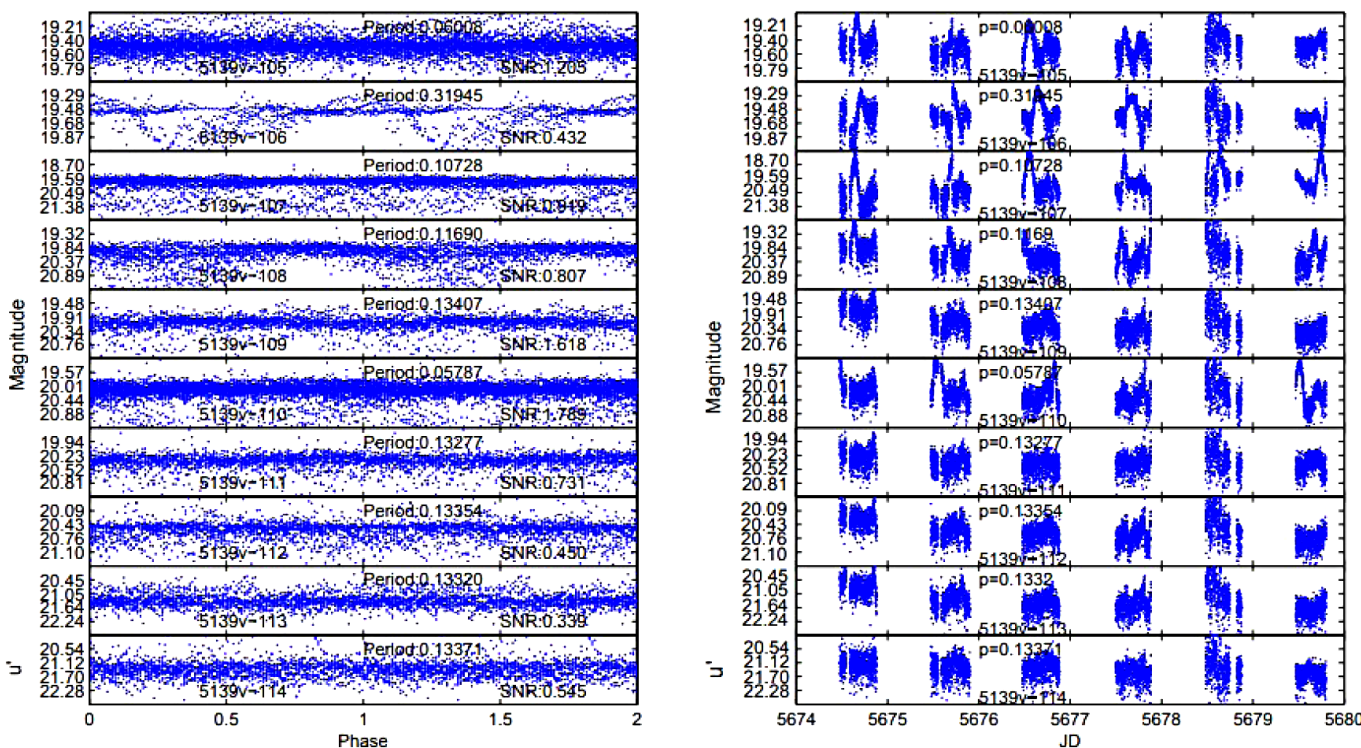


Figure B12. Phase and light curves for u' primary band for variables 5139v- 105–114. Left panel: phased light curves. Right panel: time series light curves.

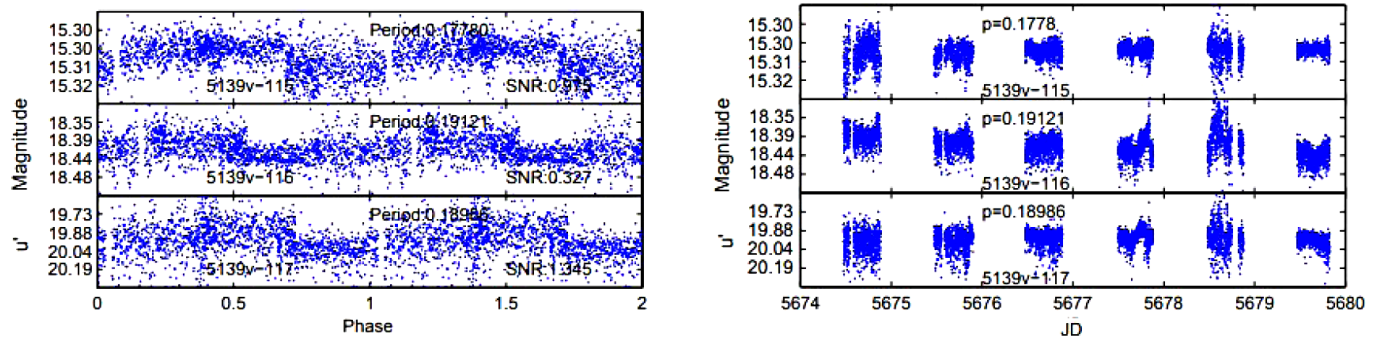


Figure B13. Phase and light curves for u' primary band for variables 5139v- 115–117. Left panel: phased light curves. Right panel: time series light curves.